Coverage-dependent structures and thermodynamic stability of intercalated Gd layers beneath buffer-layer graphene on SiC(0001)

Yong Han,[1,2,*] Shen Chen,[1,2], Marek Kolmer,[1] Lin-Lin Wang[1,2], James W. Evans,[1,2] and Michael C. Tringides,[1,2]
[1] Ames National Laboratory, U. S. Department of Energy, Ames, Iowa 50011, USA
[2] Department of Physics and Astronomy, Iowa State University, Ames, Iowa 50011, USA

ABSTRACT:

Electronic properties of two-dimensional (2D) materials are strongly influenced by their atomic arrangements, making the theoretically-aided characterization of experimentally-synthesized 2D structures crucial. Using first-principles density functional theory, we analyze nearly 200 configurations of intercalated Gd layers beneath buffer-layer graphene on SiC(0001) over a Gd coverage range of $0.01 < \theta < 1.2$. By fully relaxing selectively-constructed configurations at each coverage within a large, low-strain supercell, we determine the coverage dependence of the chemical potential for intercalated Gd structures. Thermodynamically-preferred configurations below $\theta \approx 0.8$ form single-atom-thick monolayers, while 3D-like or multilayer structures emerge beyond $\theta \approx 0.9$. Most structures are amorphous-like, including the configuration at the chemical potential minimum around $\theta \approx 0.4$. In contrast, a strongly stretched Gd(0001)-like monolayer at $\theta = 1/3$ and a nearly perfect Gd(0001) monolayer at $\theta = 1$ are significantly less favorable with 0.16 eV and 0.82 eV higher chemical potentials above the minimum, respectively. Furthermore, the graphene layer decoupled by intercalated Gd near the chemical potential minimum is significantly flatter compared to its morphology above intercalated 3D structures at higher coverages and nearly isolated Gd atoms in the lowest coverage region. These findings align with our experimental results and underscore the need for further research on this unique intercalated system, which holds significant potential for diverse applications.

Keywords:
Graphene on SiC(0001) substrate
Gd intercalation
Gd coverage dependence
First-principles DFT calculations
Thermodynamic stability
Scanning tunneling microscopy

Email:
*y27h@ameslab.gov
ORCID iDs:
Yong Han https://orcid.org/0000-0001-5404-0911
Shen Chen https://orcid.org/0000-0002-4405-8031
Marek Kolmer https://orcid.org/0000-0002-6786-9697
Lin-Lin Wang https://orcid.org/0000-0003-0965-3246
James W. Evans https://orcid.org/0000-0002-5806-3720
Michael C. Tringides https://orcid.org/0000-0001-5003-7280

1. Introduction

Producing high-quality two-dimensional (2D) heterostructures with novel electronic properties often necessitates intercalating heteroatoms into the interlayer spaces of layered materials [1, 2, 3, 4, 5, 6]. Recently, Gd-intercalated graphene on SiC(0001) has garnered significant attention, both in experimental studies [7, 8, 9, 10, 11, 12, 13] and theoretical investigations [8, 14, 10, 12], building on earlier research into the intercalation of other elements [5]. Link et al. [8] demonstrated that electron doping and strong electronic correlations in Gd-intercalated graphene on SiC(0001) can lead to the formation of flat bands, a class of materials currently attracting intense interest across various fields of physics [15]. Wang et al. [13] experimentally observed a replica Dirac cone in Gd-intercalated graphene on SiC(0001), attributed to a superlattice with a Kekulé-like distorted phase. This phase induces a bandgap opening, a key feature for quantum computing applications. Furthermore, Qu et al. [11] experimentally showed that even very low coverage of surface atoms can initiate a global Kekulé density wave phase and a bandgap opening in H- or Gd-intercalated graphene on SiC(0001).

Since the intercalated structure directly influences the electronic properties of the system, understanding the real-space structural ordering and thermodynamic stability of the intercalant is fundamentally important for applications. Previous studies employing density functional theory (DFT) have primarily focused on evaluating the band structures of Gd-intercalated buffer-layer graphene (commonly referred to as zero-layer graphene or ZLG) on Si-terminated SiC(0001) substrates [8, 14, 12], and analyzing the interactions between Gd and the graphene-SiC system [14, 12]. However, the preferred crystalline or other structures of intercalated Gd and their thermodynamic stability remain largely unexplored. In the above-mentioned studies, the coverage of the intercalated Gd monolayer is assumed to be either $\theta = 1/3$ or $\theta = 1$ in each gallery between ZLG and the Si-terminating layer (STL), or between two graphene layers for single-layer graphene (SLG) or bilayer graphene (BLG) supported on Si-terminated SiC(0001) substrates. Here, the coverage θ of intercalated Gd atoms is defined as the ratio of Gd atoms to Si atoms in the perfect STL.

The above assumptions or constraints on the selection of θ are associated with the use of small supercell sizes. However, utilizing small lateral supercells induces significant strain in graphene due to the lattice mismatch between graphene and SiC(0001) [16, 17]. Furthermore, use of smaller supercells is insufficient for analyzing amorphous-like configurations, which are often thermodynamically favorable for intercalated layers [16, 17]. Clarifying the intercalated structures at a given coverage is crucial, because the electronic properties of a 2D system are highly dependent on its structure or phase [1, 2, 3, 4, 5, 6]. For instance, a recent study demonstrated that structural disorder in an amorphized hydrogenated α-Sn(111) monolayer can induce topological electronic order in an otherwise topologically trivial crystal [18]. This finding underscores the importance of verifying the amorphization of a 2D monolayer under specific synthesis conditions as a

prerequisite for exploring its electronic properties. In this work, we will examine these aspects in detail for the Gd-intercalated system.

Another aspect of the above-mentioned DFT studies for Gd coverages of $\theta = 1/3$ [14, 12] or $\theta = 1$ [12] is the demonstration that intercalated Gd is most stable in the ZLG-STL gallery compared to other positions in ZLG [12], SLG [12], or BLG systems [14]. This behavior is analogous to that observed in Pb-intercalated graphene-SiC systems [21]. For systems with multiple graphene layers, such as SLG or BLG, the presence of various galleries provides multiple opportunities for deposited atoms to intercalate, necessitating further systematic exploration to identify all possible structures within these different galleries. However, in most rare-earth metal-intercalated systems studied so far, the experimentally observed most favorable structure, under sufficiently high annealing temperatures and at high coverage of deposited atoms, is intercalation into the ZLG-STL gallery [9, 23]. Furthermore, in previous theoretical studies [14, 12, 21], the chemical potential of an intercalated Gd or Pb monolayer in the ZLG-STL gallery shows minimal dependence on the thickness of the graphene layers, whether ZLG, SLG, or BLG. Based on these observations, we focus exclusively on the Gd-intercalated ZLG-SiC(0001) system in this study, excluding BLG and SLG configurations.

Our focus in this work is on theoretical analysis of the real-space structural ordering of intercalated Gd layers beneath ZLG on SiC(0001) for comparison with and elucidation of experimentally observed structures. To this end, we perform extensive first-principles DFT calculations to investigate the coverage dependence of these structures as well as their thermodynamic stability. In our DFT calculations, we employ a sufficiently large supercell to minimize artificially introduced strain. A larger lateral supercell size also allows us to investigate a broad range of Gd coverages, as detailed in the following sections. It is appropriate to note that DFT analysis identifies structures corresponding to stable local minima in energy, rather than in free energy, and thus strictly represents local equilibrium structures at 0 K. At temperatures above 0 K, equilibrium structures also incorporate configurational entropy (and, to a lesser extent, vibrational entropy), as typically assessed by Monte Carlo simulation for epitaxial adlayers. For adsorbed or intercalated layers where atoms are not strongly localized at specific adsorption sites, molecular dynamics simulations can provide insight into structure and dynamics [22]. However, at low liquid-nitrogen temperatures, as employed in scanning tunneling microscopy (STM) imaging of intercalated Gd layers [9,10], these entropic effects are expected to be insignificant. Indeed, the structures predicted by DFT analysis are consistent with these experimental observations. Specifically, our DFT calculations reveal a relatively weak dependence of the chemical potential on coverage for the most favored amorphous configurations, consistent with experimental observations that this disordered phase is the most stable over a wide coverage range [9,10]. Moreover, our DFT results reveal that at even higher coverages, the preferred lattice orientation of ordered subsurface Gd domains aligns with the SiC(0001) direction rather than the graphene primitive cell direction. This observation agrees with earlier experimental and theoretical studies [24, 25] on metal adsorption on graphene. These studies demonstrated that metals such as Gd and Dy preferentially orient along the SiC(0001) direction, whereas other metals tend to align with the graphene lattice direction.

From a broader perspective, 0 K DFT analysis is the standard approach for investigating intercalated layer structures of various metals beneath graphene on SiC(0001). The consistency between DFT predictions and experimentally observed structures has been frequently demonstrated [8, 10, 12, 14, 16, 17, 21, 22, 29]. Another aspect of our 0 K DFT results underscores their utility in elucidating differences in intercalation behavior between Gd and other metals. Specifically, the chemical potential of the intercalated metal (relative to its higher value for the adsorbed metal) directly correlates with the deintercalation temperature. In this study, the particularly low chemical potential found for Gd intercalation, compared to Pb, is consistent with the experimentally observed deintercalation temperature of approximately 1300 °C for Gd. This temperature is significantly higher than that for Pb deintercalation and is close to the graphitization temperature of SiC itself.

A distinct challenge lies in analyzing the kinetics of intercalated layer formation through the deposition of metal on graphene supported by SiC(0001). This process is driven by chemical potential differences between various adsorbed and intercalated Ga configurations. However, the detailed kinetics are governed by multiple diffusion barriers [19, 20, 21], which collectively control the transfer of deposited atoms from the surface to the subsurface. In contrast to Pb [16, 22], the intercalation of rare-earth elements like Gd [9, 10] or Dy [23] to form a uniform layer beneath graphene on the SiC(0001) substrate requires significantly higher temperatures, up to approximately 1200 °C. This suggests that the overall energy barrier associated with Gd or Dy intercalation exceeds that for Pb intercalation. While our previous work has characterized the kinetics of Pb intercalation [21], this contribution focuses on the challenging task of elucidating the structures of intercalated Gd and comparing them with experimental observations (where kinetics are not a factor). The kinetics of Gd intercalation will be addressed in a separate study.

The paper is organized as follows: Section 2 describes the DFT methodology and supercell selection employed in this study. Section 3 presents and discusses the DFT results. Section 4 summarizes the key findings. Appendix A provides a DFT benchmark analysis of the bulk properties of hcp Gd, Appendix B examines lattice mismatching and strain in graphene and Gd(0001) relative to SiC(0001), and Appendix C lists the DFT data for 201 configurations, including 175 Gd-intercalated configurations and 26 Gd atop adsorption configurations.

2. DFT methodology and supercell selection

All DFT calculations in this study are performed using the VASP code [26], with PAW pseudopotentials provided by the VASP group [27]. To account for van der Waals (vdW) interactions, we employ the optB88-vdW functional [28], consistent with our previous studies [29, 30, 21, 16, 17].

As discussed in Section 1, it is essential to select a supercell with a sufficiently large lateral size to comprehensively determine the coverage dependence of thermodynamically favorable structures. Based on previous experimental observations that graphene layers

grown on the SiC substrate display a $\left(6\sqrt{3}\times 6\sqrt{3}\right)R30°$ reconstruction [31 32 33], we choose a rhombic supercell to be $13a_{\mathrm{G}}^{*}\times 13a_{\mathrm{G}}^{*}$ matching $6\sqrt{3}a_{\mathrm{SiC}}\times 6\sqrt{3}a_{\mathrm{SiC}}$ [denoted as $(13\times 13)\mathrm{G}/(6\times 6)\mathrm{SiC}$; see Fig. 1a], where a_{SiC} is the lattice constant of 6*H*-SiC crystal, and a_{G}^{*} is the strained ZLG lattice constant. If we take the optB88-vdW values $a_{\mathrm{SiC}}=3.09545$ Å and freestanding graphene lattice constant $a_{\mathrm{G}}=2.464$ Å [29], the supercell corresponds to a tiny lateral tensile strain $\varepsilon_{\mathrm{G}}=(a_{\mathrm{G}}^{*}/a_{\mathrm{G}}-1)\times 100\%\approx 0.4\%$ with a strained overlayer graphene lattice constant $a_{\mathrm{G}}^{*}=6\sqrt{3}a_{\mathrm{SiC}}/13\approx 2.475$ Å. In contrast, a small supercell of $4a_{\mathrm{G}}^{*}\times 4a_{\mathrm{G}}^{*}$ matching $2\sqrt{3}a_{\mathrm{SiC}}\times 2\sqrt{3}a_{\mathrm{SiC}}$ (or $2a_{\mathrm{G}}^{*}\times 2a_{\mathrm{G}}^{*}$ matching $\sqrt{3}a_{\mathrm{SiC}}\times\sqrt{3}a_{\mathrm{SiC}}$) corresponds to a significantly larger lateral tensile strain $\varepsilon_{\mathrm{G}}=(a_{\mathrm{G}}^{*}/a_{\mathrm{G}}-1)\times 100\%\approx 8.8\%$ with $a_{\mathrm{G}}^{*}=\sqrt{3}a_{\mathrm{SiC}}/2\approx 2.681$ Å. For the lattice mismatch and strain in graphene relative to SiC(0001), also see Appendix B. Previously, these small supercells were used [8, 14, 9, 10, 12] to assess the band structures of Gd-intercalated graphene-SiC systems or the binding energies of Gd, despite the inherent introduction of a significant lateral tensile strain of approximately 8.8%. Recent studies on Pb-intercalated graphene-SiC systems [16, 17] have demonstrated a strong strain dependence of the chemical potential of intercalated Pb. Additionally, the $(13\times 13)\mathrm{G}/(6\times 6)\mathrm{SiC}$ supercell has been validated as sufficiently large for simulating amorphous-like configurations using periodic slab models [17], making it a suitable choice for this study.

In our slab calculations, the kinetic energy cutoff for planewave coefficients is set to 550 eV, and the force convergence tolerance is maintained below 0.005 eV/Å. Electric dipole corrections as well as spin polarization are also considered. The vacuum thickness perpendicular to the slab surface is kept at a minimum of 20 Å. The substrate consists of two composite C-Si layers (see, e.g., Fig. 1c or 1d), which is sufficiently thick [17]. The dangling bonds of the bottommost C atoms are always passivated using pseudo-H atoms. During the energy minimization, these bottommost C atoms are held fixed, and all other atoms are fully relaxed. The k mesh is taken to be $1\times 1\times 1$ for the large supercell. For bulk hcp Gd crystal, we obtain a lattice constant of $a_{\mathrm{Gd}}=3.595$ Å and a cohesive energy of $E_{\mathrm{coh}}=4.364$ eV using PAW Gd_3 potential. A detailed DFT benchmark analysis for bulk properties of Gd is provided in Appendix A, including discussion on the selection of functional and PAW potential.

3. DFT results and discussion

3.1. Chemical potentials

The thermodynamic stability of intercalated Gd structures beneath or adsorbed on top of ZLG can be evaluated using the chemical potential [21], defined as

$$\mu=\frac{E_{\mathrm{tot}}-E_{\mathrm{GSiC}}}{N_{\mathrm{Gd}}}-E_{\mathrm{gas,Gd}}. \tag{1}$$

Here, E_{tot} is the total energy of the entire slab containing Gd, E_{GSiC} is the energy of ZLG-SiC substrate without Gd, N_{Gd} is the total number of Gd atoms in the supercell, and $E_{\mathrm{gas,Gd}}$ is the energy of one single Gd atom in the gas phase. Alternatively, replacing the reference energy

$E_{\mathrm{gas,Gd}}$ in Eq. 1 with the energy per Gd atom (σ_{Gd}) in bulk hcp Gd crystal yields the chemical potential

$$\mu^* = \frac{E_{\mathrm{tot}} - E_{\mathrm{GSiC}}}{N_{\mathrm{Gd}}} - \sigma_{\mathrm{Gd}}. \quad (2)$$

This alternative chemical potential μ^* in Eq. 2 is equivalent to the combination energy E_{comb} previously defined [34]. For bulk hcp Gd, the chemical potential satisfies $\mu = \mu_0 \equiv \sigma_{\mathrm{Gd}} - E_{\mathrm{gas,Gd}} = -E_{\mathrm{coh}}$ and $\mu^* = 0$. The chemical potential for bulk Gd also approximately applies to large 3D Gd clusters supported on graphene. Thus, $\mu < \mu_0$ or $\mu^* < 0$ indicates a preference for deposited Gd to intercalate rather than form large supported 3D clusters, and $\mu > \mu_0$ or $\mu^* > 0$ indicates the opposite.

3.1. Intercalation and adsorption of a single Gd atom

Determining the chemical potentials of a single atom for both intercalation and adsorption is essential, as these values are among the key energetic parameters required in kinetic models for analyzing and simulating the mass transport between the top of graphene layer and the intercalated gallery during the intercalation processes [19 20]. Let us examine the case of $N_{\mathrm{Gd}} = 1$, which corresponds to the lowest possible coverage $\theta = 1/108 \approx 0.0093$ for the supercell $(13 \times 13)\mathrm{G}/(6 \times 6)\mathrm{SiC}$, given that the $\sqrt{3}a_{\mathrm{SiC}} \times \sqrt{3}a_{\mathrm{SiC}}$ unit cell includes three Si atoms in the STL. At such a low coverage, the interaction between two Gd atoms in adjacent supercell replicas is close to zero. Thus, this system allows reliable assessment of behavior for a single (or laterally isolated) Gd atom (see Fig. 1). In contrast, the lowest possible coverages are significantly higher: $\theta = 1/3 \approx 0.3333$ for the small supercell $(2 \times 2)\mathrm{G}/(1 \times 1)\mathrm{SiC}$ [8, 12] and $\theta = 1/12 \approx 0.0833$ for the supercell $(4 \times 4)\mathrm{G}/(2 \times 2)\mathrm{SiC}$ [14, 9], where the coverage is calculated [17] as $\theta = N_{\mathrm{Gd}}/N_{\mathrm{Si}}$. Here, N_{Si} is the number of Si atoms in perfect STL per supercell. For these higher coverages, the increased interactions between periodic replicas reduce the reliability of the estimates for isolated Gd atoms.

To locate the energy minima of a Gd atom intercalated beneath or adsorbed on top of ZLG, we follow our previous approach [29] by establishing a series of equidistant grid point locations within the lateral supercell. We individually relax $N = j^2$ configurations, with the Gd atom initially positioned at equidistant grid points on a 2D $j \times j$ grid covering the entire lateral area of the fully relaxed ZLG-SiC supercell (Fig. 1a). By comparing the total energies and analyzing the geometries of all configurations after full relaxation, the energy minima are identified. In principle, to reliably capture all possible minima, a larger j value is required. In this work, we set $j = 5$, which is expected to be sufficiently large (as confirmed by the final configurations listed in Tables 3 and 4 in Appendix C). Thus, we relax $N = j^2 = 25$ configurations, represented by the 25 cyan bold crosses in Fig. 1a. These configurations are labeled from 1 to 25 for the Gd atom intercalated beneath or adsorbed on top of TLG. The initial configurations with the same label for the Gd atom under and on top of TLG differ only by a shift along the direction (i.e., the height) vertical to the slab surface.

By examining the 25 final configurations for Gd intercalation after full relaxation, we find that the Gd atom always moves to a local hcp or fcc site [17] near its initial position. The average values of μ are 10.957 eV with a standard deviation of 0.032 eV at 16 hcp sites, and 11.424 eV with a standard deviation of 0.006 eV at 9 fcc sites (see Fig. 1b and Table 3), indicating that all these configurations are highly unfavorable. The small but non-zero standard deviations reflect the inequivalence of these hcp or fcc sites due to the complex and varying epitaxial relationships within the (13×13)G/(6×6)SiC supercell. The most favorable case with the lowest μ among these 25 configurations is illustrated in Fig. 1c. The top ZLG has a corrugation of $c = 0.90$ Å with local bending around the position of the Gd atom. The corrugation c is defined as the height difference between the highest and lowest C atom within the graphene layer [29]. This corrugation value is smaller than $c_0 = 1.39$ Å for the pristine ZLG-SiC system, indicating that the intercalation of the Gd atom can flatten ZLG. The total interlayer spacing between ZLG and STL is $d = d_1 + d_2 = 1.63 + 2.09 = 3.72$ Å (see Fig. 1c), which is 1.27 Å larger than $d_0 = 2.45$ Å for the pristine ZLG-SiC system due to the intercalation of the Gd atom (i.e., a steric effect), where d_1, d_2, and d are the interlayer spacings between Gd layer and ZLG, between Gd layer and STL, and between ZLG and STL, respectively. Here, an interlayer spacing is defined as the difference of average heights of atoms between two corresponding layers.

As a comparison, we examine 25 final configurations of Gd adsorption on top of graphene after full relaxation, where the final position of the Gd atom strongly depends on its initial position (see Table 4). The average value of μ is -3.503 eV with a standard deviation of 0.445 eV (see Fig. 1b and Table 3). The relatively large standard deviation in μ reflects the roughness of the ZLG surface, as shown in Fig. 1d, where the most favorable configuration, corresponding to the lowest μ, is illustrated. The top ZLG layer exhibits a corrugation of $c = 1.16$ Å, where some C atoms in a C ring are displaced upward or downward relative to the planar surface. This corrugation is larger than the above $c = 0.90$ Å observed for intercalation but smaller than $c_0 = 1.39$ Å. The interlayer spacing between ZLG and the STL is 2.37 Å (see Fig. 1d), which is close to $d_0 = 2.45$ Å due to the absence of steric effects in the adsorption case.

As shown in Fig. 1b, the μ values (> +10 eV) for intercalation are all positive and much higher than the bulk value of $\mu_0 = -4.364$. Consequently, the intercalation of a single Gd atom is extremely unfavorable compared to Gd in its bulk crystal form or even in the gas phase. The likely reason for the unfavorability is that for a single Gd atom to intercalate beneath ZLG, multiple strong C-Si covalent bonds must be broken, leading to a substantial increase in the total energy of the system. This bond breaking is evident from the increase in interlayer spacing from $d_0 = 2.45$ Å for the pristine ZLG-SiC system to 3.72 Å (see Fig. 1c). This reflects the transition of C atoms in ZLG from sp^3 bonding with the substrate to sp^2 bonding, characteristic of a decoupled-like graphene layer [35]. Meanwhile, the Si atoms in the STL is left with numerous dangling bonds. The μ values for adsorption, averaging around -3.503 eV, are negative but still significantly higher than the bulk value of $\mu_0 = -4.364$ eV. Therefore, adsorption on top of ZLG is more favorable than the gas phase of Gd

but less favorable than the bulk Gd crystal. Nonetheless, adsorption is vastly more favorable than intercalation due to the significant chemical potential difference of $+10.936 - (-4.283) = 15.219$ eV (see Figs. 1c and 1d).

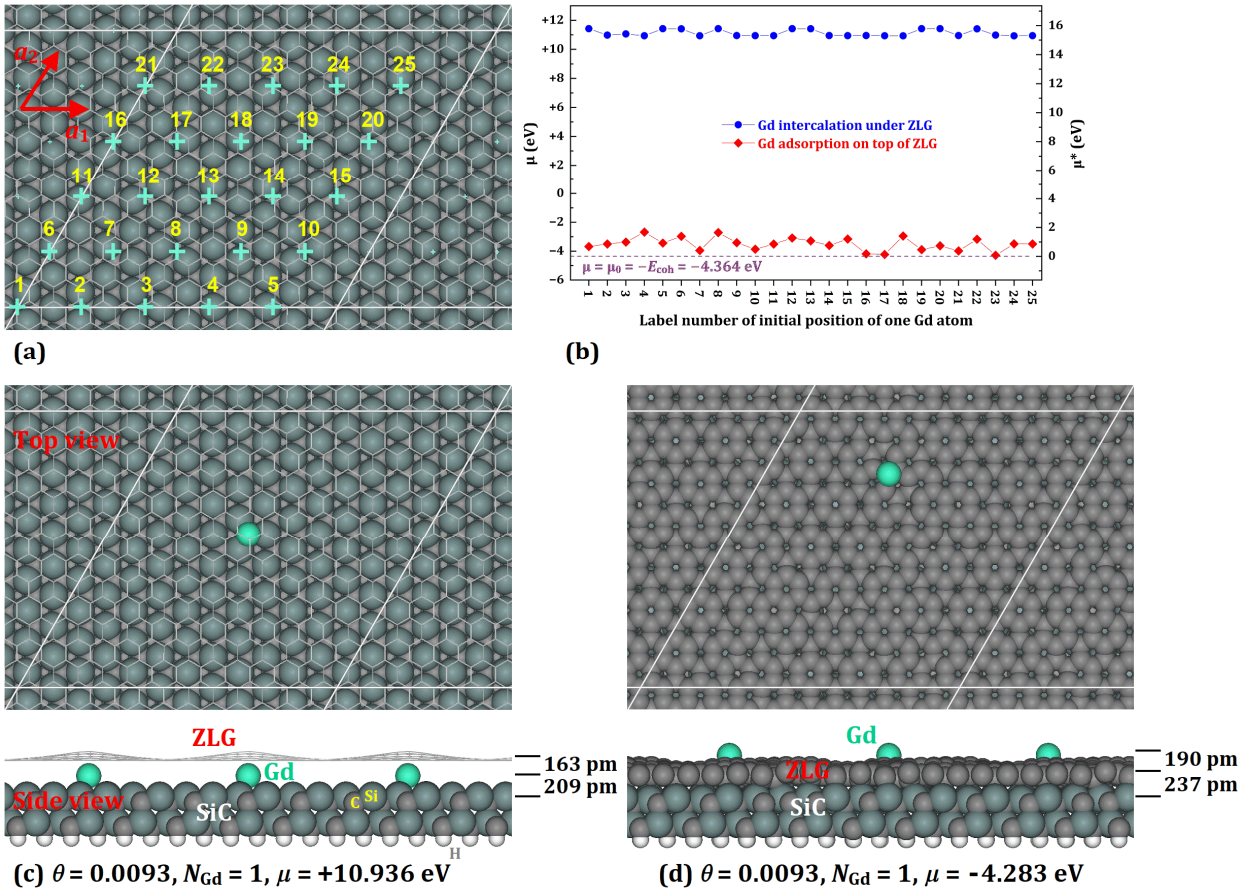

Fig. 1. (1) Top view of ZLG on Si-terminated SiC(0001). A white rhombus indicates the lateral size of a (13 × 13)G/(6 × 6)SiC supercell. $\boldsymbol{a_1}$ and $\boldsymbol{a_2}$ are the directions of two lateral translation vectors of the supercell. The 25 cyan bold crosses indicate initial positions of a single Gd atom for intercalation under ZLG or adsorption on top of ZLG within a supercell. (b) Chemical potentials of the Gd atom after fully relaxing the 25 initial positions for intercalation or adsorption. The purple horizontal line indicates the chemical potential $\mu = \mu_0 = -E_{\text{coh}} = -4.364$ eV (i.e., $\mu^* = 0$) for bulk hcp Gd crystal from our DFT calculation. (c) Top and side views of the most favorable configuration (the 18th in (b)) for the single Gd atom intercalated under ZLG per supercell. (d) Top and side views of the most favorable configuration (the 23rd in (b)) for the single Gd atom adsorbed on top of ZLG. In (a) and (d), ZLG appears as thin gray hexagonal mesh for clarity. The values of corresponding Gd coverage θ, number (N_{Gd}) of Gd atoms per supercell, and chemical potential μ are also indicated in (c) and (d). The two interlayer spacings d_1 and d_2 (in pm) above STL are indicated in (c) or (d). Similar statements apply to all the following figures and will no longer be repeated. For more details, see the text as well as Tables 3 and 4 in Appendix C.

3.2. Intercalation of Gd in low coverage region

For a given $N_{\mathrm{Gd}} > 1$, we adopt the following strategy to search for the global energy minimum. We construct an intercalated Gd initial configuration using one or more Gd monolayers. Each Gd monolayer is uniformly arranged as a Gd array along the $\boldsymbol{a_1}$ and $\boldsymbol{a_2}$ directions (see Fig. 1), forming a 2D Bravais lattice with a $6\sqrt{3}a_{\mathrm{SiC}}/n_1 \times 6\sqrt{3}a_{\mathrm{SiC}}/n_2$ rhombic primitive cell containing n_{p} Gd atoms. If $n_1 = n_2 = l$ and $n_{\mathrm{p}} = 1$, the $l \times l$ Gd array corresponds to a hcp Gd(0001) plane with a lattice constant of $a_0^* = 6\sqrt{3}a_{\mathrm{SiC}}/l$. The intercalated Gd slab consists of L stacked $n_1 \times n_2$ Gd planar monolayers, and then $N_{\mathrm{Gd}} = n_1 n_2 L n_{\mathrm{p}}$. For a given set of the parameters N_{Gd}, $n_1 \times n_2$, L, and n_{p}, we relax three different initial configurations, which are sufficient to obtain an approximate global minimum (see below). Any two of these three initial configurations involve a collective lateral shift, which is selected according to the local symmetry, e.g., we choose a small shift of $a_{\mathrm{SiC}}/3$ along the $\boldsymbol{a_1}$ direction, etc. In this work, we select and fully relax 175 intercalated Gd initial configurations. These initial configurations are determined by the parameter sets, where three different initial configurations for a given parameter set (N_{Gd}, $n_1 \times n_2$, L, and n_{p}) are identified by the different labels, as listed in Table 3. In the following Figs. 2–7 (except Fig. 3), we only plot the most favorable configuration, i.e., the one with the lowest μ value, among all fully relaxed configurations for a given N_{Gd} or coverage θ. In this subsection, we focus on small N_{Gd}, i.e., low θ region.

Let us first consider the case of $N_{\mathrm{Gd}} = 4$ ($\theta \approx 0.0370$). In contrast to $\mu > +10$ eV for the configurations of $N_{\mathrm{Gd}} = 1$ (Fig. 1), the most prominent feature of the configuration in Fig. 2a is that μ is dramatically reduced to -1.943 eV, even though the coverage slightly increases by only $0.0370 - 0.0093 = 0.0277$. As shown in Fig. 2a, the corrugation of the decoupled ZLG decreases to 0.74 Å from 0.90 Å in Fig. 1c, indicating a decrease in elastic energy due to less bending and stretching in ZLG. This reduction in corrugation could be the main reason for the significant decrease in μ. Another possible factor contributing to the decrease in μ could be the decrease in the interatomic Gd-Gd distance. However, this contribution is expected to be very weak [36, 37, 38, 39] due to the still large Gd-Gd separation of $a_0^* = 3\sqrt{3}a_{\mathrm{SiC}} \approx 16$ Å. The total interlayer spacing between ZLG and STL is $d = d_1 + d_2 = 1.91 + 2.08 = 3.99$ Å, which is sufficient large to decouple ZLG. We also note that from $N_{\mathrm{Gd}} = 1$ to $N_{\mathrm{Gd}} = 4$, the Gd-STL spacing d_2 remains almost constant at about 2 Å. The increase in the total interlayer spacing d is primarily due to the contribution $\Delta d_1 = 1.91 - 1.63 \approx 0.3$ Å, indicating that ZLG becomes more decoupled as the Gd coverage increases. This results in reduced bending and stretching within the ZLG.

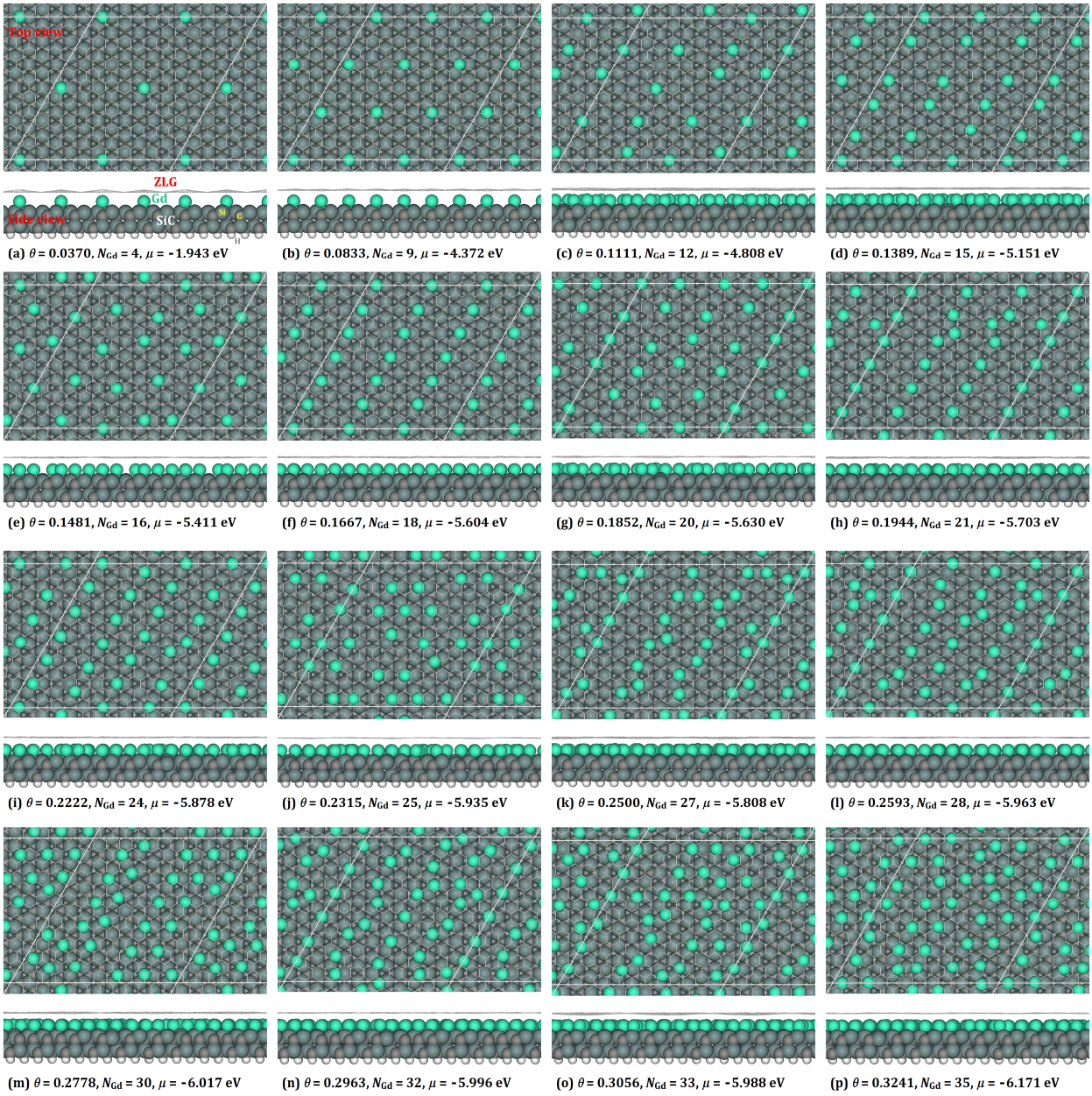

Fig. 2. Top and side views of fully relaxed configurations for intercalated Gd in the coverage range from $\theta \approx 0.0370$ to 0.3241 ($N_{\mathrm{Gd}} = 4$ to 35 per supercell) from our DFT calculations. For more details, see the text as well as Table 3 in Appendix C.

As θ increases, the μ value continues to decrease significantly. For $N_{\mathrm{Gd}} = 9$, 12, 15, 16, 18, 20, 21, 24, 25, 27, 28, 30, 32, 33, and 35 (or $\theta \approx 0.0833$, 0.1111, 0.1389, 0.1481, 0.1667, 0.1852, 0.1944, 0.2222, 0.2315, 0.2500, 0.2593, 0.2778, 0.2963, 0.3056, and 0.3241), the μ values are -4.372, -4.808, -5.151, -5.411, -5.604, -5.630, -5.703, -5.878, -5.935, -5.808, -5.963, -6.017, -5.996, -5.988, and -6.171 eV, respectively (also see Fig. 2). In this low θ region, μ decreases rapidly at first and then begins to decrease more gradually (see olive dots plotted in Fig. 3). Simultaneously, d_1 continues to increase and gradually stabilizes around $d_0 = 2.45$ Å, while d_2 only slightly rises to approximately 2.2 Å (see Fig. 4). Along with this, the corrugation c steadily decreases and eventually stabilizes, albeit with fluctuations. The upper limit of c is 0.53 Å at $N_{\mathrm{Gd}} = 33$, while the lower limit drops to 0.24 Å at $N_{\mathrm{Gd}} = 32$ (see again Fig. 4), indicating a very flat decoupled ZLG sheet (see the side views in Fig. 2).

As discussed above, the decrease in μ may result from reduced bending and stretching within the ZLG sheet. However, at higher coverages, where Gd-Gd intralayer separations decrease, attractive Gd-Gd interactions also contribute to lowering μ. At the lowest θ, the reduced bending and stretching of ZLG is the dominant factor, but as the coverage increases, the influence of Gd-Gd interactions gradually takes over.

The arrangement of atoms in a fully relaxed intercalated Gd layer generally depends on its initial configuration. However, the chemical potential is not highly sensitive to the chosen configurations for a given coverage (as shown by the olive dots and dark cyan circles in Fig. 3). Therefore, the strategy discussed above for finding the global energy minimum serves as a good approximation. As shown in Fig. 2, at very low coverage, the fully relaxed configurations of Gd atoms remain relatively close to their initial regular $n_1 \times n_2$ arrangements, though some local distortions or movements may occur. As the coverage increases, the configuration tends to become more amorphous-like, driven by stronger interactions between Gd atoms and by the geometric asymmetry within the supercell.

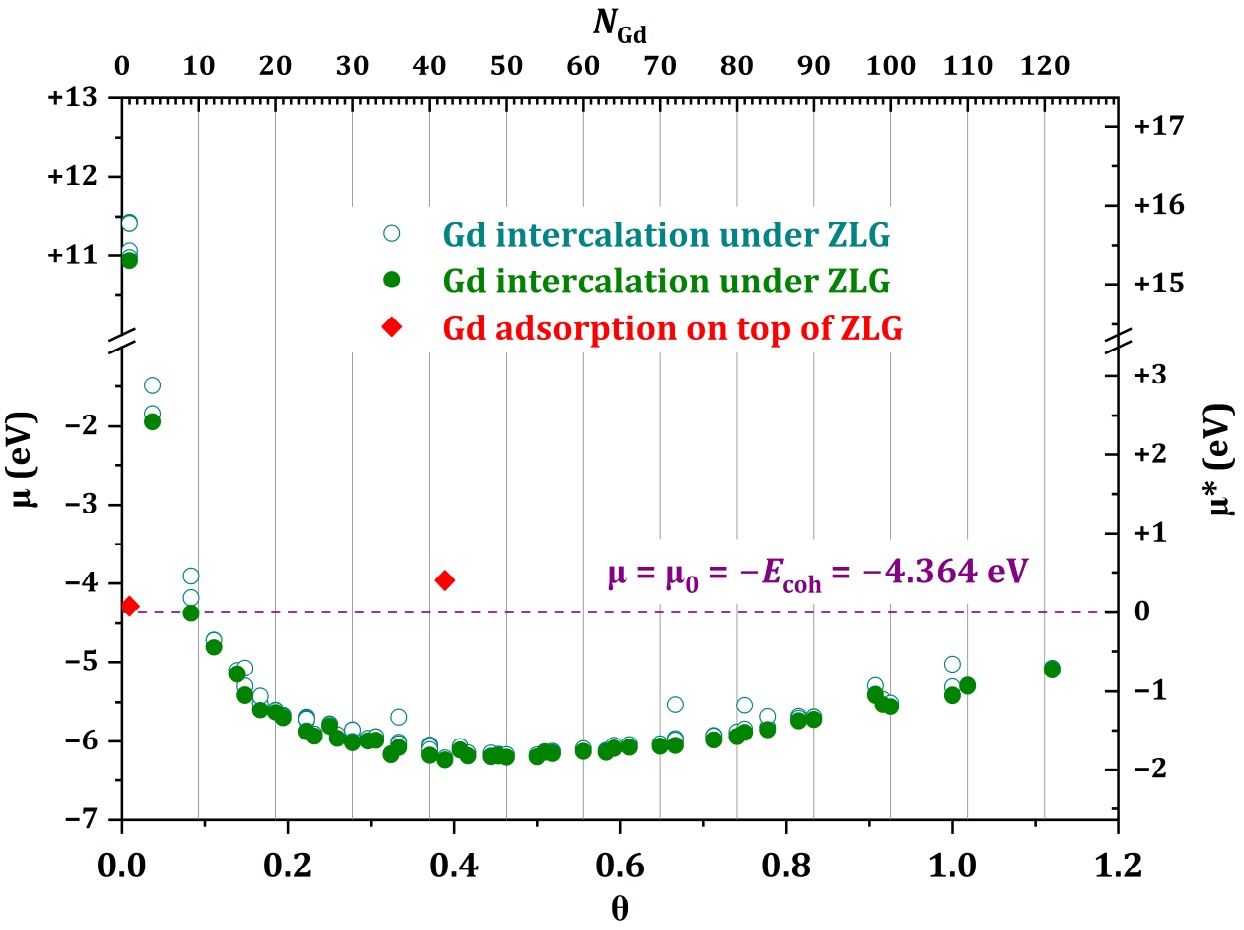

Fig. 3. DFT chemical potentials (μ or μ^*) of 175 intercalated Gd structures (olive dots and dark cyan circles) within the Gd coverage (θ) range from about 0.01 to 1.12 (or N_{Gd} from 1 to 121). An olive dot corresponds to the most favorable configuration with the lowest μ value at a given θ, and dark cyan circles correspond to other configurations with higher μ values. The red diamonds correspond to two configurations of Gd adsorbed on top of ZLG at $\theta \approx 0.0093$ ($N_{Gd} = 1$) and $\theta \approx 0.3889$ ($N_{Gd} = 42$).

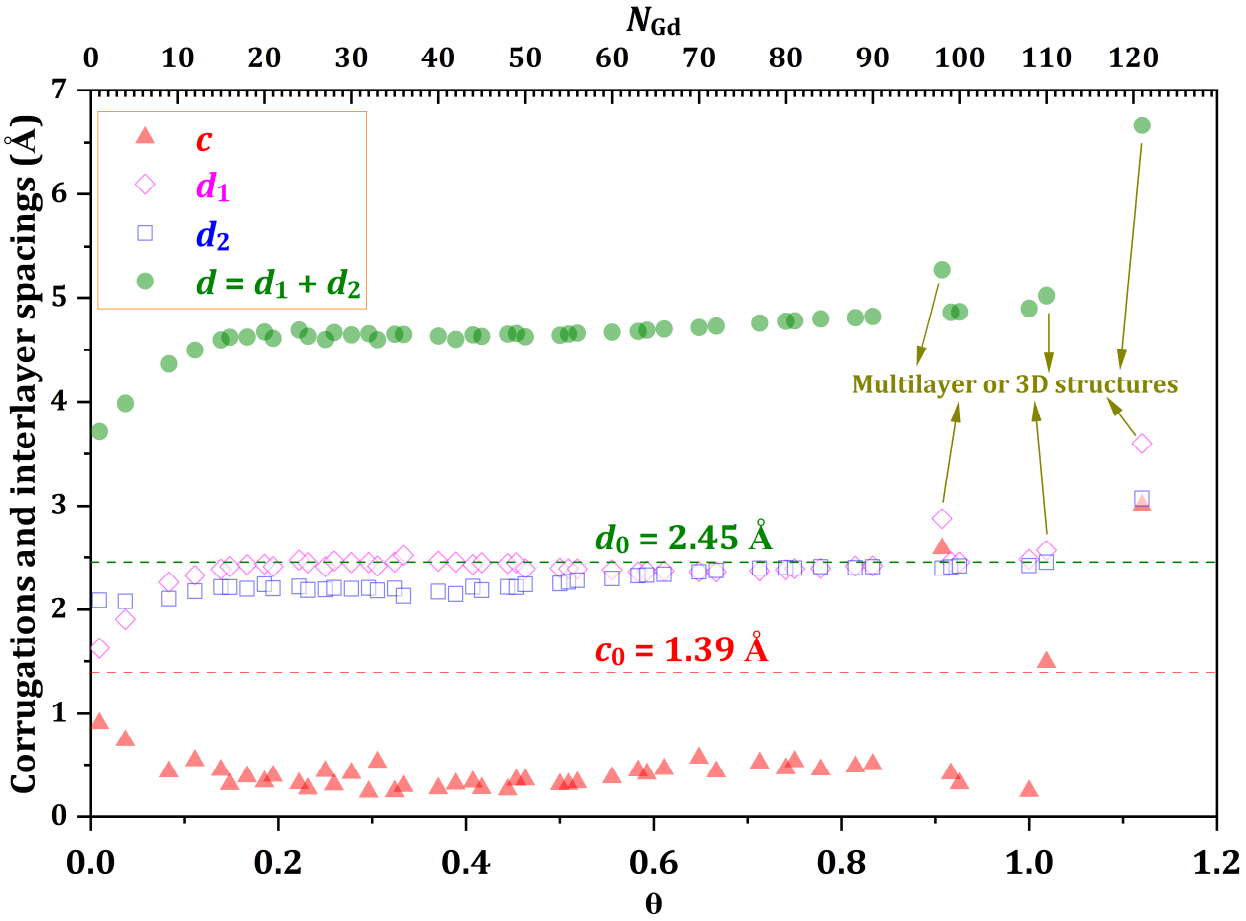

Fig. 4. Decoupled ZLG corrugations (c) and interlayer spacings of 46 configurations with intercalated Gd structures within the Gd coverage (θ) range from about 0.01 to 1.12 (or N_{Gd} from 1 to 121) from our DFT calculations. d_1, d_2, and $d = d_1 + d_2$ are the interlayer spacings between Gd and ZLG, between Gd and STL, and between ZLG and STL, respectively. Red and olive horizontal dashed lines represent the ZLG corrugation $c_0 =$ 1.39 Å and the ZLG-STL interlayer spacing $d_0 = 2.45$ Å for pristine ZLG-SiC system from our DFT calculations, respectively. The dark yellow arrows indicate the data points corresponding to multilayer or 3D structures of intercalated Gd at $N_{Gd} = 98$, 110, and 121, while all other data points correspond to intercalated Gd monolayer.

3.3. Intercalation and adsorption of Gd in intermediate coverage region

As mentioned above, earlier DFT calculations have analyzed Gd coverage of $\theta = 1/3$ in the STL-ZLG gallery using small supercells like $(4 \times 4)\mathrm{G}/(2 \times 2)\mathrm{SiC}$ [14] or $(2 \times 2)\mathrm{G}/(1 \times 1)\mathrm{SiC}$ [12], which introduces significant lateral tensile strain of approximately 8.8%. In addition, such small supercell sizes restrict the investigation of potential amorphous-like structures of intercalated Gd. In this study, we utilize a much larger supercell $(13 \times 13)\mathrm{G}/(6 \times 6)\mathrm{SiC}$ with a minimal lateral tensile strain of about 0.4% to explore the resulting structures. The coverage of $\theta = 1/3$ corresponds to $N_{\mathrm{Gd}} = 36$ when the supercell $(13 \times 13)\mathrm{G}/(6 \times 6)\mathrm{SiC}$ is used. We relax six initial configurations, where the intercalated Gd monolayer is arranged as an $n_1 \times n_2 = 6 \times 6$ array for three configurations, and as an $n_1 \times n_2 = 4 \times 9$ array for the other three configurations. The fully relaxed final configurations are listed in Table 3, where configurations labeled 036-01, 036-02, and 036-03 come from the 6×6 array, while 036-04, 036-05, and 036-06 come from the 4×9 array. Two of these (036-01 and 036-02) exhibit a nearly perfect 6×6 Gd monolayer structure, but 036-02 has a notably lower μ, with a difference of $(-5.695) - (-6.078) = 0.383$ eV compared to 036-01. In this context, the 6×6 Gd monolayer corresponds to a hcp Gd(0001) plane with a strongly stretched lattice constant $a_0^* = \sqrt{3}a_{\mathrm{SiC}} \approx 5.36$ Å (relative to our DFT values of $a_0 = 3.384$ Å for a freestanding Gd(0001) monolayer and $a_{\mathrm{Gd}} = 3.595$ Å for bulk hcp Gd. See Appendix A), where the orientation of the primitive cell of the perfect hcp Gd(0001) plane is aligned with the $\left(\sqrt{3} \times \sqrt{3}\right)R30°$ orientation of the SiC(0001) surface (see Fig. 5a). Thus, we denote this nearly perfect 6×6 Gd array as a strongly stretched Gd(0001)-like monolayer. For more information about lattice mismatch and strain in Gd(0001) relative to SiC(0001), see Appendix B. Configuration 036-03 appears amorphous-like, with a slightly higher μ by only $(-6.066) - (-6.078) = 0.012$ eV than 036-02. The μ values for the remaining three configurations, 036-04, 036-05, and 036-06, are -6.032 eV, -6.014 eV, and -6.033 eV, respectively, all quite close to -6.078 eV for 036-02, and these are also amorphous-like configurations. Therefore, the amorphous-like configurations (036-03, 036-04, 036-05, and 036-06) and the strongly stretched Gd(0001)-like configuration 036-02 are effectively energetically degenerate. Among these six configurations, we only plot the configuration with the lowest μ, i.e., 036-02, as shown in Fig. 5a.

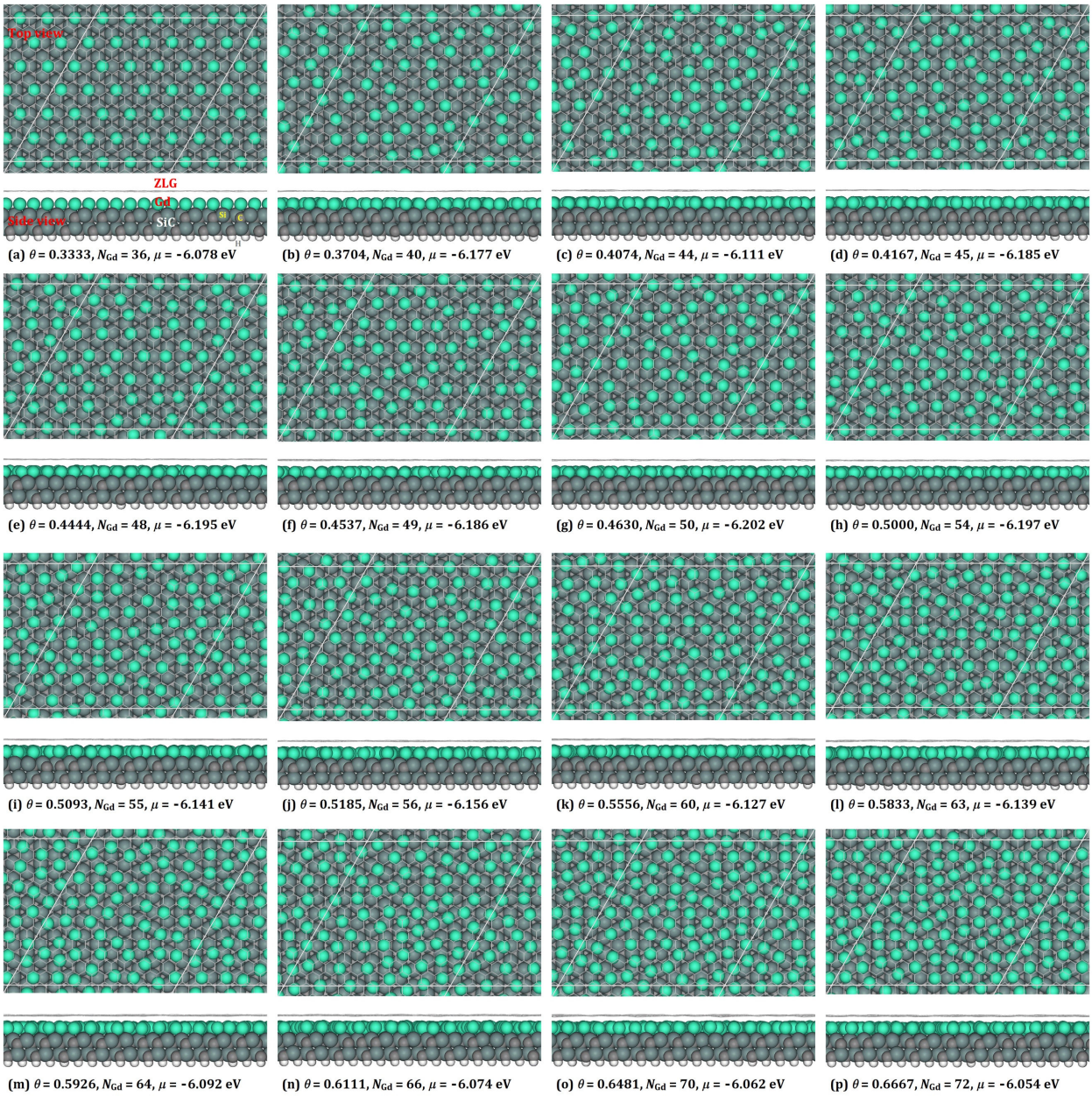

Fig. 5. Top and side views of fully relaxed configurations for intercalated Gd in the coverage range from $\theta \approx 0.3333$ to 0.6667 ($N_{\mathrm{Gd}} = 36$ to 72 per supercell) from our DFT calculations. For more details, see the text as well as Table 3 in Appendix C.

For any intermediate coverage in the range of $1/3 < \theta \leq 2/3$, we find that the fully relaxed final configuration of Gd with the lowest chemical potential, μ, always exhibits an amorphous-like monolayer structure, as shown in Fig. 5. The average value of μ for the 17 configurations (including 16 from Fig. 5 and one from Fig. 6a) in this range is -6.142 eV, with a small standard deviation 0.056 eV. This indicates a narrow distribution of μ, spanning from -6.238 eV to -6.054 eV (see olive dots in Fig. 3). The minimum μ of -6.238 eV is found at $N_{\mathrm{Gd}} = 42$ ($\theta \approx 0.3889$) and the corresponding configuration is separately plotted in Fig. 6a. Notably, the strongly stretched Gd(0001)-like monolayer at $\theta = 1/3$ (plotted in Fig. 5a) has a chemical potential approximately 0.16 eV higher than this minimum, highlighting the substantial difference in thermodynamic favorability (relative to bulk Gd crystal or large 3D Gd clusters formed on top of ZLG surface) between these two structures. Additionally, two other configurations at $N_{\mathrm{Gd}} = 42$ also exhibit low μ values of -6.219 eV and -6.212 eV, both of which are very close to the minimum value of -6.238 eV

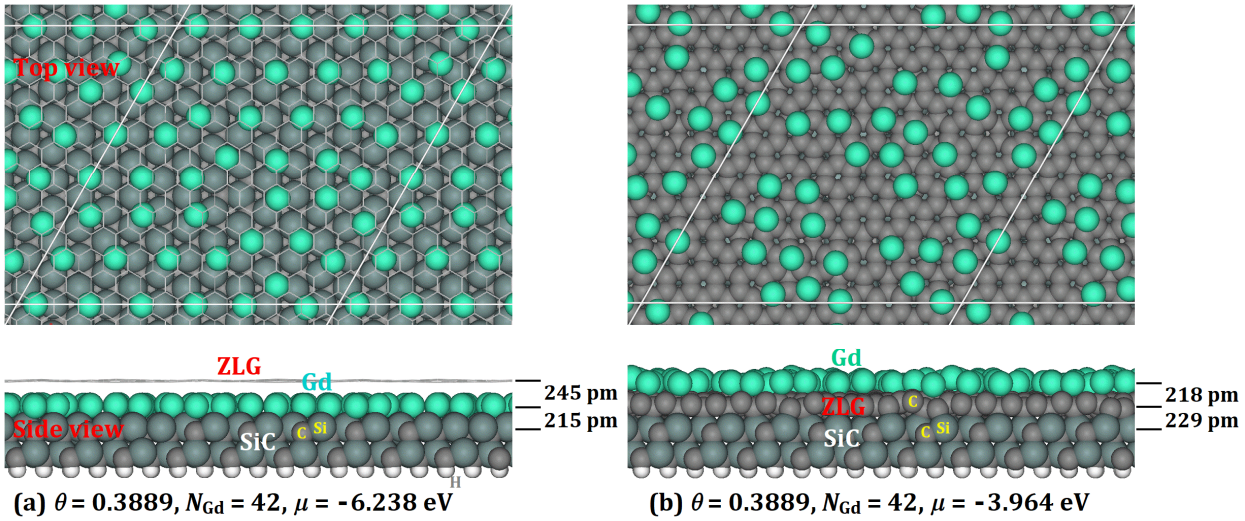

(a) θ **= 0.3889,** N_{Gd} **= 42,** μ **= -6.238 eV** **(b)** θ **= 0.3889,** N_{Gd} **= 42,** μ **= -3.964 eV**

(Table 3).

Fig. 6. Top and side views of fully relaxed configurations for a Gd monolayer (a) intercalated under ZLG and (b) adsorbed on top of ZLG at the coverage $\theta \approx 0.3889$ ($N_{\mathrm{Gd}} = 42$ per supercell) from our DFT calculations. The chemical potential of the configuration in (a) is the lowest one among all configurations in this work. For more details, see the text as well as Tables 3 and 4 in Appendix C.

For $N_{\mathrm{Gd}} = 72$ (coverage $\theta = 2/3$), we relax six initial configurations (listed in Table 3). In the configurations labeled 072-01, 072-02, and 072-03, the intercalated Gd monolayer is arranged as a 6×6 honeycomb (gadolinene) monolayer, which forms an $n_1 \times n_2 = 6 \times 6$ array, with the number of Gd atoms in a primitive cell being $n_{\mathrm{p}} = 2$. The purpose of this setup is to determine the stability of such a gadolinene layer. After full relaxation, we find that the Gd monolayer in 072-02 retains its initial gadolinene structure, while the Gd monolayers in 072-01 and 072-03 transform into amorphous-like structures. However, the chemical potential μ of 072-02 is -5.534 eV, which is significantly higher than the values $\mu = -6.014$ eV for 072-01 and $\mu = -6.027$ eV for 072-03, indicating that the intercalated

gadolinene monolayer in 072-02 is highly unstable and unlikely to be experimentally observed. In contrast, the intercalated Gd monolayers in 072-04, 072-05, and 072-06 are arranged as 8×9 arrays, with $n_{\mathrm{p}} = 1$ Gd atom in the primitive cell. After full relaxation, all three of these Gd monolayers become amorphous-like, with chemical potentials of $\mu = -6.054$ eV, -5.968 eV, and -5.986 eV, respectively. Therefore, 072-04, which has the lowest chemical potential, is illustrated in Fig. 5p.

The average of corrugations (c) for the 17 configurations in this coverage region is 0.36 Å, with a small standard deviation of 0.08 Å, indicating that each decoupled ZLG sheet remains very flat. In this same coverage region, the interlayer spacing d_1 gradually decreases from 2.52 Å to 2.36 Å, while d_2 slowly increases from 2.13 Å to 2.37 Å, and they tend to equalize as the coverage increases. The average value of the total interlayer spacings ($d = d_1 + d_2$) for these 17 configurations is 4.66 Å, with a small standard deviation of 0.03 Å, indicating that d remains essentially constant. See Fig. 4 for these trends. For the most favorable configuration (illustrated in Fig. 6a), the interlayer spacing is $d = d_1 + d_2 = 2.454 + 2.151 \approx 4.605$ Å.

For a limited comparison of intercalated and absorbed configurations, we select just one initial configuration for adsorption with $\theta = 0.3889$ by shifting the intercalated amorphous-like Gd monolayer from Fig. 6a to sit atop ZLG. The fully relaxed final configuration is shown in Fig. 6b, which is highly unfavorable with a significantly higher μ value of -3.964 eV relative to the intercalated configuration in Fig. 6a. This value is even higher than $\mu = -4.283$ eV for a single Gd atom adsorption, shown in Fig. 1d (see the two diamond symbols in Fig. 3). The increase in μ reflects the complex competition between intralayer Gd-Gd interactions and interlayer Gd-ZLG interactions for the atop adsorption. The substrate-mediated interactions (including pair and other many-body interactions [36, 37, 38, 39]) are not monotonically decreasing functions of Gd-Gd separations. The chemical potential difference between intercalation (Fig. 6a) and adsorption (Fig. 6b) for $\theta = 0.3889$ is $(-6.238) - (-3.964) = 2.274$ eV. This value can be compared with a value of 2.02 eV from recent DFT calculations using a small supercell of (2×2)G/(1×1)SiC at the coverage of $\theta = 1/3$ for the ZLG-SiC system [12], as well as a difference of 3.06 eV from DFT calculations with a small supercell of (4×4)G/(2×2)SiC for the BLG-SiC system at $\theta = 1/3$ [14]. Moreover, in Fig. 6b, the Gd atoms have significantly rearranged compared to the initial Gd monolayer in Fig. 6a. The interlayer spacing between the top Gd layer and ZLG is 2.18 Å, and the ZLG-STL interlayer spacing is 2.29 Å, which is slightly smaller than the pristine ZLG-SiC system value of $d_0 = 2.45$ Å.

3.4. Intercalation of Gd in higher coverage region

As shown in Fig. 3, with the continuing increase of intercalated Gd coverage θ, the chemical potential μ begins to slowly rise from its minimum of -6.238 eV at $N_{\mathrm{Gd}} = 42$ ($\theta \approx 0.3889$) and continues until it reaches -5.099 eV at $N_{\mathrm{Gd}} = 121$ ($\theta \approx 1.1204$), which marks the upper limit of the coverage considered in this work. Simultaneously, as shown in Fig. 7, the amorphous-like intercalated Gd monolayer progressively becomes more locally

ordered. In these locally ordered regions (as illustrated by a yellow hexagon in Fig. 7f), the arrangement of Gd atoms resembles a hcp Gd(0001)-like monolayer structure, where the orientation of the hcp (0001) primitive cell (shown as the yellow rhombus in Fig. 7j) aligns with the SiC(0001) primitive cell. Additionally, multilayer or intercalated 3D Gd structures may emerge at higher coverages, as detailed below.

At $N_{\mathrm{Gd}} = 108$ ($\theta = 1$), we take a 6×6 Gd array with $n_{\mathrm{p}} = 3$, which is equivalent to a $6\sqrt{3}a^*_{\mathrm{Gd}} \times 6\sqrt{3}a^*_{\mathrm{Gd}}$ Gd(0001) monolayer. In this arrangement, the unit cell $\sqrt{3}a^*_{\mathrm{Gd}} \times \sqrt{3}a^*_{\mathrm{Gd}}$ aligns with the $\sqrt{3}a_{\mathrm{SiC}} \times \sqrt{3}a_{\mathrm{SiC}}$ unit cell of the SiC(0001) substrate. There is a 30° rotation between the $\sqrt{3}a^*_{\mathrm{Gd}} \times \sqrt{3}a^*_{\mathrm{Gd}}$ unit cell and its primitive cell with the lattice constant of $a^*_{\mathrm{Gd}} = a_{\mathrm{SiC}}$. Since $a_{\mathrm{SiC}} = 3.09545$ Å is smaller than the lattice constant $a_0 = 3.384$ Å for a freestanding Gd(0001) monolayer, the $6\sqrt{3}a^*_{\mathrm{Gd}} \times 6\sqrt{3}a^*_{\mathrm{Gd}}$ Gd(0001) monolayer is compressed by about 8.5 % relative to the freestanding monolayer. This $6\sqrt{3}a^*_{\mathrm{Gd}} \times 6\sqrt{3}a^*_{\mathrm{Gd}}$ Gd(0001) monolayer is used as the initial intercalated Gd configuration for 108-01, 108-02, or 108-03. After full relaxation, a nearly perfect $6\sqrt{3}a^*_{\mathrm{Gd}} \times 6\sqrt{3}a^*_{\mathrm{Gd}}$ Gd(0001) monolayer is obtained (listed in Table 3). Among these, the configuration 108-02 has the lowest μ value of -5.415 eV and is illustrated in Fig. 7j. In this figure, the $\sqrt{3}a^*_{\mathrm{Gd}} \times \sqrt{3}a^*_{\mathrm{Gd}}$ unit cell and its primitive cell of the intercalated Gd(0001) monolayer are marked by the red and yellow rhombi, respectively, indicating the orientation and alignment of the Gd(0001) structure relative to the SiC substrate. This configurations contrasts with an intercalated $\sqrt{3}a^*_{\mathrm{Gd}} \times \sqrt{3}a^*_{\mathrm{Gd}}$ Gd(0001) monolayer used in previous DFT calculations [8 12] which employed a small supercell of (2×2)G/(1×1)SiC at the coverage $\theta = 1$. Compared to the chemical potential minimum found at $N_{\mathrm{Gd}} = 42$ ($\theta \approx 0.3889$) in Fig. 6a, the configuration in Fig. 7j exhibits a significant chemical potential increase of 0.823 eV, underscoring the substantial difference in thermodynamic favorability (e.g., relative to a large 3D Gd cluster on top of ZLG surface) between these two structures.

To assess the favorability of a potential intercalated Gd bilayer in the not-too-high coverage range, we focus on two different coverages. For the first one, since the chemical potential minimum for intercalated Gd monolayers occurs at $N_{\mathrm{Gd}} = 42$, we explore the possibility of forming an intercalated Gd bilayer by relaxing a configuration with $N_{\mathrm{Gd}} = 42 \times 2 = 84$ ($\theta \approx 0.7778$). This bilayer consists of two stacked monolayers arranged in a 6×7 Gd array, i.e., $n_1 \times n_2 = 6 \times 7$, $L = 2$, and $n_{\mathrm{p}} = 1$. Upon full relaxation, configurations 084-01 and 084-02 both collapse into a monolayer structure, while configuration 084-03 forms a slightly bumped monolayer (as listed in Table 3). The μ values for configurations 084-01 and 084-02 are -5.855 eV and -5.825 eV, respectively, which are significantly lower than the μ value of -5.688 eV for 084-03. These results suggest that a monolayer structure is more energetically favorable than bilayer or 3D structures at this coverage. The configuration 084-01, which has the lowest μ value among the three configurations, is illustrated in Fig. 7d.

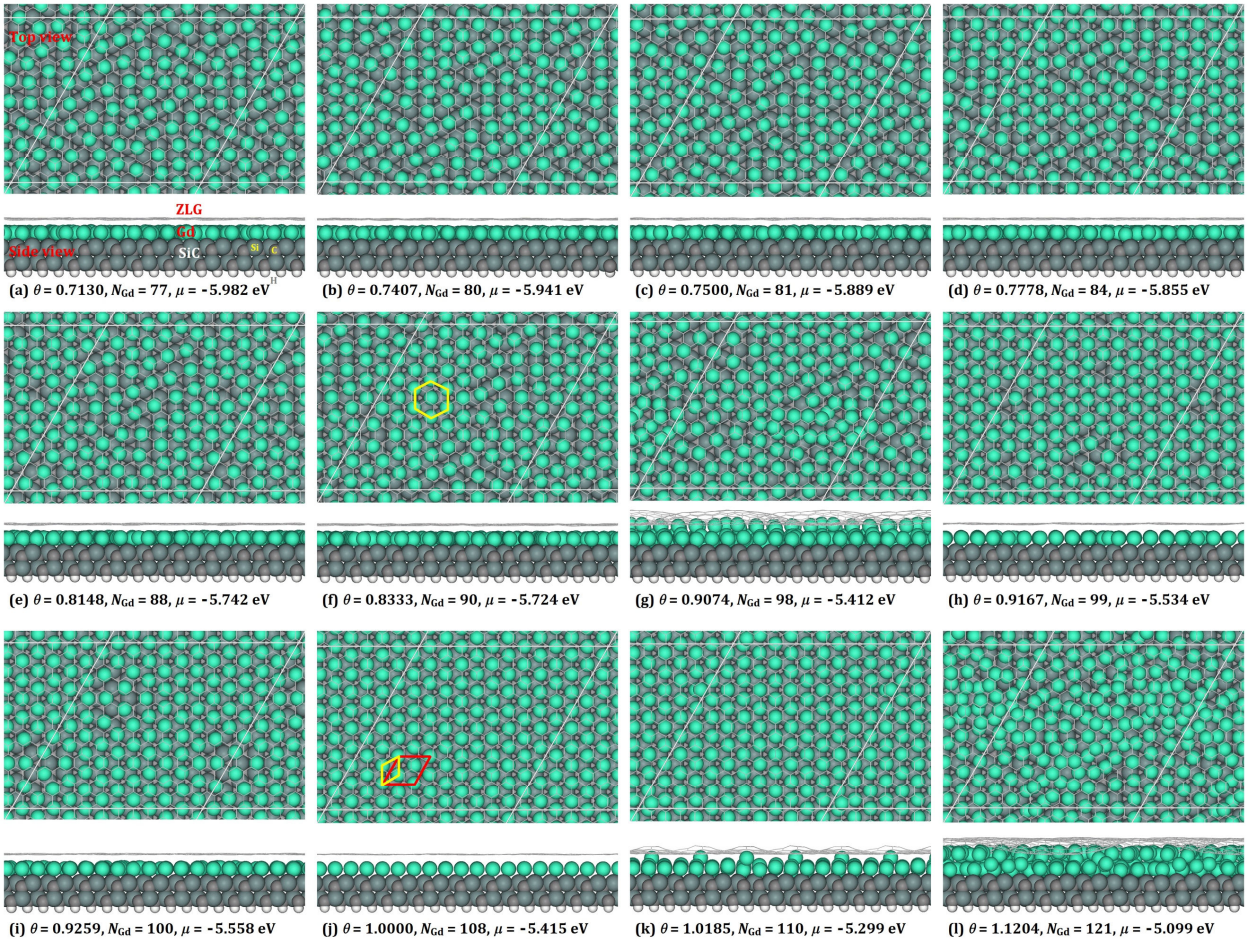

Fig. 7. Top and side views of fully relaxed configurations for intercalated Gd in the coverage range from $\theta \approx 0.7130$ to 1.1204 ($N_{\mathrm{Gd}} = 77$ to 121 per supercell) from our DFT calculations. A yellow hexagon in (f) indicates the local regular order. The red and yellow rhombi in (j) indicate the $\sqrt{3}a^*_{\mathrm{Gd}} \times \sqrt{3}a^*_{\mathrm{Gd}}$ unit cell and the corresponding primitive cell of a Gd(0001) monolayer, respectively. For more details, see the text as well as Table 3 in Appendix C.

For the second coverage, we relax a configuration with $N_{\mathrm{Gd}} = 49 \times 2 = 98$ ($\theta \approx 0.9074$). This bilayer consists of two stacked monolayers arranged in a 7×7 Gd array, i.e., $n_1 \times n_2 = 7 \times 7$, $L = 2$, and $n_{\mathrm{p}} = 1$. Upon full relaxation, configuration 098-01 collapses into a Gd(0001)-like monolayer structure with some 3D bumps, while configurations 098-02 and 098-03 form locally bumped Gd(0001)- or amorphous-like monolayers (as listed in Table 3). The configuration 098-03, which has the lowest μ value of -5.412 eV among the three configurations, is illustrated in Fig. 7g. We note that this μ value of -5.412 eV is 0.122 eV higher than the μ value of -5.534 at $N_{\mathrm{Gd}} = 99$ ($\theta \approx 0.9167$) in Fig. 7h, which slightly deviates from the expected monotonic increase in μ with increasing θ in this region. A possible explanation for this deviation is that the relaxation of only three initial configurations does not yield a fully 2D-like Gd monolayer structure. It is likely that a 2D-like Gd monolayer with a lower μ value than -5.412 eV could be achieved by relaxing more initial configurations or by employing alternative strategies for constructing the initial configurations. For instance, removing one specific Gd atom from the fully relaxed configuration at $N_{\mathrm{Gd}} = 99$ in Fig. 7h, which features a Gd(0001)-like monolayer with vacancies, could be an effective approach, as was previously demonstrated for Pb intercalation [17].

At $N_{\mathrm{Gd}} = 110$ ($\theta \approx 1.0185$), we relax three initial configurations, with the intercalated Gd monolayer arranged in a 10×11 Gd array. After relaxation, the initially perfect Gd monolayer in each configuration transforms into a Gd(0001)-like monolayer featuring 3D bumps (as listed in Table 3). The μ values for configurations 110-01, 110-02, and 110-03 are closely clustered: -5.299 eV, -5.298 eV, and -5.292 eV, respectively, indicating that these configurations are effectively energetically degenerate. The configuration 110-01 is illustrated in Fig. 7k. The appearance of these 3D bumps suggests that a Gd monolayer structure at this higher coverage ($\theta > 1$) may no longer be thermodynamically favorable.

Finally, let us examine the structure at $N_{\mathrm{Gd}} = 121$ ($\theta \approx 1.1204$), the upper limit of the coverage considered in this work. We relaxed three initial configurations with the intercalated Gd monolayer arranged in an 11×11 Gd array. After relaxation, the initially perfect Gd monolayer in each configuration transformed into a complex 3D structure (referred to as an amorphous-like multilayer) without a regular crystalline pattern (listed in Table 3). The μ values for configurations 121-01, 121-02, and 121-03 are quite close: -5.099 eV, -5.078 eV, and -5.083 eV, respectively, indicating that these configurations are effectively energetically degenerate. The configuration 121-01 is illustrated in Fig. 7l. These amorphous-like multilayer structures suggest that forming a 2D-like Gd monolayer structure at such high coverage ($\theta \gtrsim 1.1$) may no longer be feasible.

The interlayer spacings for configurations with a Gd monolayer structure in the higher coverage region remain relatively constant, with an average value of $= d_1 + d_2 = 2.41 + 2.41 = 4.82$ Å, and an insignificant standard deviation of less than 0.05 Å. The corresponding corrugations in decoupled ZLG have an average of 0.44 Å with a standard deviation of 0.10 Å, reaching a minimum of 0.247 Å at $N_{\mathrm{Gd}} = 108$ ($\theta = 1$), as shown in Fig. 4. For configurations with a 3D or multilayer Gd structure at $N_{\mathrm{Gd}} = 98$, 110, or 121, both

the interlayer spacing and the corrugation increase significantly due to the steric effects, varying strongly depending on the specific intercalated Gd structure, as indicated by arrows in Fig. 4 as well as by the side views in Figs. 7g, 7k, and 7l.

3.5. Discussion for Gd coverage dependence

As analyzed above, the construction of the initial intercalated Gd monolayer is based on a uniformly arranged $n_1 \times n_2$ Gd planar array. When $n_1 = n_2 = l$, the resulting $l \times l$ Gd array corresponds to a strained hcp Gd(0001) layer. The lateral lattice constant of this hcp (0001) monolayer is given by $a_0^* = 6\sqrt{3}a_{\mathrm{SiC}}/l$, which is generally not equal to the equilibrium lattice constant $a_0 = 3.384$ Å for a freestanding Gd(0001) monolayer, leading to a lateral strain in the Gd(0001) monolayer due to the lattice mismatch with the SiC substrate. The extent of this strain depends on the value of l, as this determines the degree of compression or stretching imposed on the Gd(0001) layer. As listed in Table 2 of Appendix B, for $l \leq 9$, the strain $\varepsilon_{\mathrm{Gd}}$ exceeds +6%, a significant positive strain, where the Gd(0001) monolayer is stretched. In such cases, after full relaxation, a Gd monolayer should be expected due to this lateral stretching. On the other hand, for $l \geq 10$, the strain $\varepsilon_{\mathrm{Gd}}$ becomes less than -5%, indicating significant negative strain. This negative strain implies compression of the Gd(0001) layer, and after relaxation, a 3D Gd structure or multilayer is expected to form. These expectations align well with the structural results discussed in the above subsections.

For small l and low θ, the large Gd-Gd separation means that the weak Gd-Gd interactions have minimal influence during the relaxation of Gd atoms. In such cases (e.g., $l = 1$ or 2), the Gd atoms in an initial configuration tend to migrate to hcp or fcc sites adjacent to their initial positions, driven primarily by the Gd-substrate interactions rather than by Gd-Gd interactions. For a larger l (e.g., $l = 4$, 5, 7, and 8) and higher θ, the Gd-Gd interactions become stronger, typically leading to a significant rearrangement of the Gd atoms during relaxation. Due to the inherently low symmetry of the ZLG-SiC interface within the supercell, the Gd atoms may organize into more disordered structures, potentially resulting in the formation of an amorphous-like monolayer. This structural disorder reflects the difficulty in achieving a well-ordered Gd monolayer under these conditions. In few cases (e.g., $l = 6$), the Gd-Gd and Gd-substrate interactions in the initial configuration nearly already reach an overall balance. This balance allows for the formation of a regular but strongly stretched Gd(0001) monolayer, which remains relatively close to the initial configuration after relaxation. For $l = 9$ or 10, the strained lateral lattice constant a_0^* approaches the equilibrium lattice constant a_0. In this scenario, the stronger Gd-Gd interactions become more dominant over the Gd-substrate interactions, leading to significant rearrangement of the Gd atoms during relaxation. This rearrangement facilitates the emergence of a local regular order, where the $\sqrt{3}a_{\mathrm{Gd}}^* \times \sqrt{3}a_{\mathrm{Gd}}^*$ structure aligns with the $\sqrt{3}a_{\mathrm{SiC}} \times \sqrt{3}a_{\mathrm{SiC}}$ unit cell of the SiC(0001) substrate. Equivalently, this alignment can be expressed as $a_{\mathrm{Gd}}^* \times a_{\mathrm{Gd}}^*$ aligning with $a_{\mathrm{SiC}} \times a_{\mathrm{SiC}}$, resulting in a lattice constant a_{Gd}^* that is approximately equal to a_{SiC}. For $l > 10$ (e.g., $l = 11$), a_0^* is significantly

smaller than a_0. In this case, the strong compression within the initial Gd monolayer can cause some Gd atoms to move upward, leading to the formation of a 3D or multilayer structure of Gd.

The chemical potential μ of an intercalated Gd structure is controlled by both Gd-Gd and Gd-substrate interactions. From the chemical potential curve plotted in Fig. 3, Gd intercalation at very low coverage ($\theta \lesssim 0.1$) is thermodynamically unfavorable, with μ significantly higher than, or close to, the bulk Gd value $\mu_0 = -E_{\mathrm{coh}} = -4.364$ eV (equivalently, with μ^* significantly higher than, or closer to, zero). Consequently, Gd intercalation in this range is expected to be experimentally unobservable, as the formation of large supported 3D islands is favored. The most favorable Gd intercalation condition occurs around $\theta \approx 0.4$, where μ reaches its lowest values, indicating energetically stable configurations. Also, at higher coverages ($\theta \gtrsim 0.8$), the μ values remain significantly lower than μ_0. Thus, Gd intercalation at all coverages $\theta \gtrsim 0.1$ is energetically favorable and, therefore, expected to be experimentally observable.

3.6. Experimental observations for intercalated Gd

In Fig. 8, we present a sequence of experimental STM images illustrating the progression from room-temperature deposition to high-temperature annealing for Gd-intercalated BLG on a SiC(0001) substrate. Initially, Gd adsorbed on the graphene surface is expected to diffuse to entry portals at domain boundaries, where Gd atoms can move into subsurface galleries. The existence of domain boundaries in graphene has been experimentally confirmed [40, 41, 42, 43]. These boundaries separate regions with different bonding characteristics, weakening the sp^2 bonding across them [40], which consequently lowers the diffusion barriers for Pb adatoms to move downward into the subsurface [21]. Our previous experiments demonstrate that both Gd [9,10] and Dy [23] exhibit similar intercalation kinetics. Gd or Dy transfers from the top of graphene to below at relatively high temperatures, ranging from 900 °C to 1200 °C. Extensive discussion has been provided on the similar subsurface morphologies of the intercalated phases [9, 10, 23], where no defects are introduced in our approach to avoid deteriorating the electronic properties of graphene. For Gd or Dy deposited on graphene, domain boundaries are the most likely locations for the adatoms to diffuse downward into the surface. A future goal of our experimental and theoretical work is to measure and calculate the controlling barriers for this process.

The experiments employ successive stepwise increases in temperature to ensure the intercalated Gd spreads away from the entry portals, enabling newly arriving Gd atoms to diffuse from the top to the subsurface layers and form a spatially uniform intercalated layer. Key parameters influencing the mass transfer of Gd include the initial deposited amount, the annealing temperature, and the duration at each temperature step. At room temperature, Gd deposition with a coverage of three nominal monolayers results in the formation of 3D fractal islands on the surface, as shown in Fig. 8(a). This behavior occurs because Gd diffusion across the graphene surface and around the peripheries of Gd islands is significantly hindered at low temperatures [44, 45]. The classification of metals into strongly and weakly interacting groups for metal adsorption on graphene has been extensively studied and provides valuable insights into the growth morphologies observed

after deposition [25, 46]. These studies help explain the distinct diffusion and clustering behaviors of Gd observed during the initial stages of intercalation.

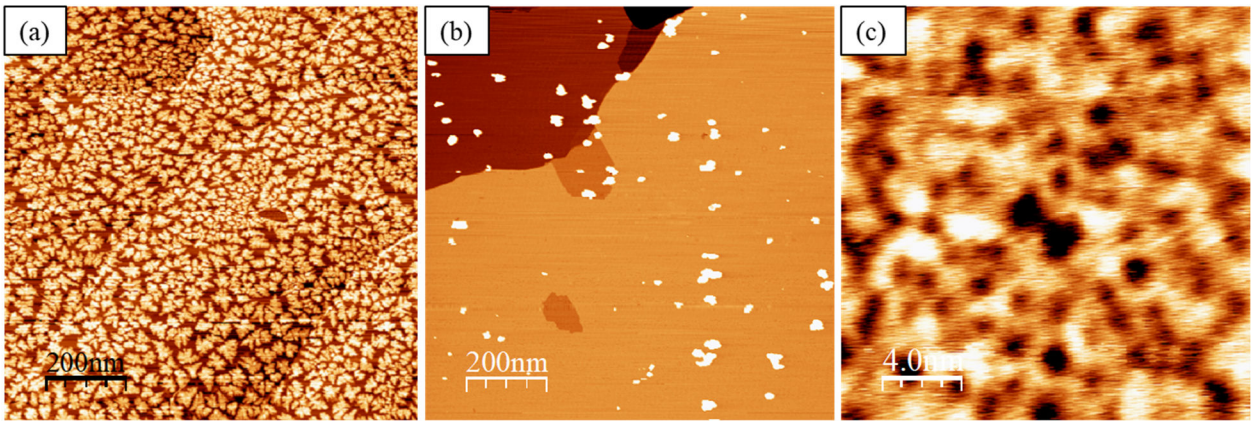

Fig. 8. (a) STM image (1000 nm × 1000 nm) showing a high density of fractal 3D islands formed after Gd deposition on BLG supported by SiC(0001) at room temperature. Island structure is attributed to the slow diffusion of Gd on graphene and around Gd island peripheries. (b) STM image (1000 nm × 1000 nm) after stepwise annealing up to 1200°C, illustrating the decay and dissolution of the fractal islands and the migration of Gd to the subsurface region. (c) High-resolution STM image (21 nm × 21 nm) of a small area from (b), highlighting the uniform, disordered intercalated phase and the absence of the well-known 6 × 6 periodicity characteristic of pristine graphene.

The outcome at the highest temperature of 1200 °C, following stepwise annealing through intermediate temperatures, is shown in Fig. 8(b) over a large 1 × 1 μm^2 area. This process produces a highly uniform subsurface Gd phase. Most of the surface is bare, with the high density of fractal Gd islands from earlier stages no longer present. A small number of stable 3D Gd islands remain on the surface, appearing as white blobs and covering only a minor fraction of the area. A high-resolution image of a smaller 21 × 21 nm^2 area showing the morphology after Gd intercalation is presented in Fig. 8(c). Pristine graphene typically exhibits a well-known moiré 6 × 6 phase, arising from the interaction between the buffer layer and SiC. However, this periodicity is completely removed after Gd intercalation, confirming the absence of long-range order in the intercalated phase. The intercalated Gd occupies the two bottommost galleries of the BLG, with the ZLG-SiC gallery being the most stable. The morphology is highly homogeneous, with a random-like distribution of Gd atoms in a gallery, indicating that the intercalated phase is highly disordered. These conclusions are supported by excellent agreement between the dI/dV maps from STM, ARPES spectra, and DFT electronic structure analysis, by assuming that the intercalated Gd occupies the two bottommost galleries [9, 10].

The basic features observed in experiments for Gd intercalation are similar to those for Dy intercalation, as demonstrated in our previous work [23]. Both the growth conditions and phase morphologies exhibit common characteristics for Gd and Dy, including the annealing temperature range (850–1200 °C) and the stability of the intercalated phases in the galleries. The final stable phase for both metals is practically indistinguishable in terms of crystal structure, as they are noncrystalline and highly uniform. These conclusions are supported by complementary techniques: surface diffraction, which probes mesoscale

morphology, and STM, which provides atomic-resolution insights into local changes.

It is interesting to compare the results for higher Gd coverage. The yellow unit cell in Fig. 7(j) highlights that intercalated Gd forms an almost periodic arrangement before the onset of bilayer formation (e.g., that shown in Fig. 7(l)). This alignment follows the SiC(0001) lattice rather than the graphene lattice due to the stronger interaction between Gd and SiC. This observation aligns with previous experimental and theoretical studies of metal adsorption on graphene. For example, SPA-LEED and STM studies of Dy adsorption on graphene-SiC(0001) substrates revealed a 3D morphology, where the Dy lattice aligns with the SiC(0001) rather than the graphene direction [24]. Extensive calculations of various metals adsorbed on graphene-SiC substrates also support these findings [25, 46]. They confirm that both Dy and Gd preferentially align with the SiC(0001) lattice direction. This is consistent with the present calculations, which show that at large coverages, subsurface binding of these metals is dominated by the aggregation of metal atoms into clusters.

4. Conclusion

In conclusion, we have conducted extensive first-principles DFT calculations to investigate the structures of intercalated Gd layers beneath the ZLG on SiC(0001). These calculations used a large (13×13)G/(6×6)SiC supercell, allowing us to explore diverse intercalated layer structures over a wide range of Gd coverages from $\theta \approx 0$ to 1.2. The large supercell minimizes the strain ($\varepsilon_{\mathrm{G}} \approx +0.4\%$) of the ZLG relative to the SiC(0001) substrate, in contrast to previous DFT studies that used smaller supercells and considered limited coverages (only $\theta = 1/3$ and 1).

Our results show that the intercalation of a single Gd atom is thermodynamically highly unfavorable compared to adsorption on top of the ZLG. At very low coverages ($\theta \lesssim 0.1$), the chemical potential μ remains higher than the bulk Gd value μ_0, making intercalation unfavorable compared to formation of large supported 3D islands. As θ increases, μ decreases steadily and reaches its minimum around $\theta \approx 0.4$, indicating that the most favorable intercalation occurs in this coverage range. At higher coverages ($\theta \gtrsim 0.8$), the μ values remain significantly lower than the bulk Gd value μ_0 as well as the μ values for Gd adsorbed on top of the ZLG. This suggests that Gd intercalation is energetically favorable and experimentally observable at all coverages $\theta \gtrsim 0.1$.

We also find that at coverages below $\theta \approx 0.9$, Gd intercalates as a monolayer structure. Above $\theta \approx 0.9$, a 3D-like or multilayer Gd structure may emerge, although a monolayer around $\theta = 1$ can still be energetically favorable. For the most favorable coverage range near $\theta \approx 0.4$, the intercalated Gd layers generally exhibit amorphous-like structures, except in few cases, such as $\theta = 1/3$, where a strongly stretched Gd(0001)-like monolayer forms with a primitive cell identical to the $\sqrt{3}a_{\mathrm{SiC}} \times \sqrt{3}a_{\mathrm{SiC}}$ unit cell of SiC(0001). At higher coverages around $\theta = 1$, the primitive cell of regular local Gd(0001)-like monolayers aligns with the $a_{\mathrm{SiC}} \times a_{\mathrm{SiC}}$ primitive cell of SiC(0001). The chemical potentials of the strongly stretched Gd(0001)-like monolayer at $\theta = 1/3$ (Fig. 5a) and a nearly perfect Gd(0001)

monolayer at $\theta = 1$ (Fig. 7j) are approximately 0.16 eV and 0.82 eV higher than that of the amorphous-like Gd monolayer at $\theta \approx 0.3889$ (Fig. 6a) This indicates that, relative to large supported 3D structures, forming these intercalated Gd(0001)-like structures at $\theta = 1/3$ or 1 are thermodynamically significantly less favorable than forming the intercalated amorphous-like structure at $\theta \approx 0.3889$. At the highest coverage considered in this study ($\theta \approx 1.12$), the intercalated Gd forms a multilayer with an amorphous-like structure.

As Gd coverage increases, the corrugation of the decoupled ZLG above the intercalated Gd monolayer decreases rapidly and stabilizes within the range of approximately 0.24 Å to 0.57 Å, down from a maximum value of about 0.90 Å at the lowest coverage, for which intercalated Gd atoms are nearly isolated. This reduction in corrugation indicates that the decoupled ZLG becomes much flatter than the pristine ZLG, which has a corrugation of 1.39 Å. Concurrently, the interlayer spacing d increases rapidly and stabilizes between approximately 4.6 Å and 4.9 Å, up from a minimum value of about 3.7 Å at the lowest coverage. Similarly, the interlayer spacing d_1 stabilizes between approximately 2.4 Å and 2.5 Å, increasing from a minimum value of about 1.6 Å, while d_2 stabilizes between approximately 2.13 Å and 2.42 Å, up from a minimum value of about 2.1 Å. These findings are illustrated in Fig. 3.

These DFT results are consistent with earlier experimental observations for Gd (and Dy, which exhibits similar behavior). For instance, the most stable high-coverage intercalated phase is disordered, and the preferred lattice orientation of the metal aligns with the SiC(0001) lattice [9, 23, 24, 25, 44]. Unlike other metals such as Pb [21, 16], the intercalation of rare-earth metals like Gd and Dy requires high temperatures, suggesting higher intercalation barriers (which have not yet been calculated in this study), despite the significantly lower chemical potentials observed in the studied coverage range. This motivates the need for a comprehensive theoretical analysis of the kinetic behavior of Gd intercalation, including the various diffusion barriers. We emphasize the importance of further research into this unique system to enable the synthesis of phases with tailored properties. Such phases hold significant potential for a variety of applications, and continued investigation will provide deeper insights into the system, facilitating the development of novel materials.

Declaration of Competing Interest

The authors declare that they have no known competing financial interests or personal relationships that could have appeared to influence the work reported in this paper.

Data availability

Data will be made available on request.

Acknowledgments

Y. H., S. C., M. K., L.-L. W, and M. C. T. were supported by the Materials Sciences and Engineering Division, and J. W. E. by the Chemical Sciences, Geosciences, and Biological Sciences Division, Computational and Theoretical Chemistry program, of the U. S. Department of Energy (USDOE), Office of Science, Basic Energy Sciences. The research was performed at the Ames National Laboratory which is operated for the USDOE by Iowa State University under contract No. DE-AC02-07CH11358. DFT calculations were performed with a grant of computer time at the National Energy Research Scientific Computing Center (NERSC). NERSC is a USDOE Office of Science User Facility supported by the Office of Science of the USDOE under Contract No. DE-AC02-05CH11231.

Appendix A: DFT benchmark analysis for bulk properties of hcp Gd

Using the DFT method described in Section 2, we achieved good agreement between the calculated bulk properties of 6*H*-SiC [29] and graphene or graphite [43] with their corresponding experimental values. Here, we examine the bulk properties of hcp Gd to verify the reliability of the DFT method. In our DFT calculations, we use the primitive cell containing two Gd atoms. The *k* mesh is taken to be $51 \times 51 \times 51$ and the cutoff energy is 550 eV, which is significantly larger than the default value 256.472 eV in Gd POTCAR and 154.332 eV in Gd_3 POTCAR for PAW potentials. This guarantees the high computational accuracy. As listed in Table 1, the lattice constants, cohesive energies, and bulk modulus from our optB88-vdW calculations (as well as from our PBE calculations as a comparison) using two PAW potentials for Gd can be in good agreements with the experimental values. Note that 4f electrons in PAW Gd_3 potential are frozen in the core, and then Gd is nonmagnetic with the magnetic moment $m = 0$, while the magnetic moments $m = 7.69\mu_B$ (PBE) and $7.59\mu_B$ (optB88-vdW) can well reproduce experimental value $7.98\mu_B$ (see Table 1) when PAW Gd potential with the 4f-electrons outside the core is used. It is well known that when PAW potentials are applied to materials containing lanthanide elements (such as Dy, Gd, Eu, etc.) with f-valence electrons, achieving total energy convergence is generally challenging or may not be possible, largely due to self-interaction errors in the strongly localized orbitals. Thus, we choose PAW Gd_3 potential because we do not analyze magnetic properties in this work, as already been widely applied previously [44].

Table 1. Bulk properties of hcp Gd from our DFT calculations, compared with available experimental values. a_{Gd} or c_{Gd} is the lattice constant of bulk hcp Gd. m is the magnetic moment in unit of Bohr magneton μ_B per Gd atom. B_0 and B_0' are the bulk modulus and the first derivative of the bulk modulus with respect to pressure, respectively. The cohesive energy is $E_{coh} = E_{gas,Gd} - \sigma_{bulk}$, where $E_{gas,Gd}$ is the energy of a single Gd atom in its gas phase, and σ_{bulk} is the energy per Gd atom in its bulk hcp phase.

Method	a_{Gd} (Å)	c_{Gd} (Å)	m (μ_B)	B_0 (GPa)	B_0'	E_{coh} (eV)
DFT, PBE, PAW Gd	3.648	5.836	7.69	35.00	3.7	3.916
DFT, optB88-vdW, PAW Gd	3.603	5.760	7.59	34.69	2.5	3.999
DFT, PBE, PAW Gd_3	3.644	5.722	0	38.03	3.1	4.227
DFT, optB88-vdW, PAW Gd_3	3.595	5.672	0	41.24	3.4	4.364
Experiments	3.629±0.002[a]	5.796±0.004[a]	7.98±0.05[b]	38.32[c]		3.55[d]
	3.6360±0.0009[e]	5.7826±0.0006[e]				4.14[f]

[a]Ref. [49] At 106 K.
[b]Ref. [50].
[c]Ref. [51].
[d]Ref. [52].
[e]Ref. [53].
[f]Ref. [54].

Using the above DFT method with the PAW Gd_3 potential, we also obtain a lattice constant of $a_0 = 3.384$ Å for a freestanding Gd(0001) monolayer by setting the *k* mesh to $61 \times 61 \times 1$ and a vacuum thickness of 30 Å between two monolayer replicas. Notably, this value of $a_0 = 3.384$ Å is significantly smaller than its bulk counterpart $a_{Gd} = 3.595$ Å. This

reduction in lattice constant is commonly observed for freestanding close-packed slabs with a few monolayers, as previously reported for Pb(111) [17] and Cu(111) [47]. When dealing with lattice mismatching between such a thin layer and its substrate, extra care must be taken in selecting an appropriate lattice constant. This is crucial, as the mismatching can significantly affect the structural stability and properties of the system, particularly in systems with few monolayers where atomic interactions and strain effects are more pronounced.

Appendix B: Lattice mismatching and strain in graphene and Gd(0001) relative to SiC(0001)

In our model for calculating systems of graphene (or ZLG) on Si-terminated SiC(0001) with (or without) intercalated Gd, we consistently fix the equilibrium lattice constant a_{SiC} of the SiC(0001) substrate. We take a_{SiC} to be our DFT-calculated value of 3.09545 Å [29], even though the intercalation of a Gd layer introduces two interfaces, the graphene-Gd interface and the Gd- STL interface, that can induce strain. This approach simplifies the analysis, as it treats the substrate lattice as rigid, allowing us to focus on how the intercalation affects the structures above the substrate, while recognizing that strain is induced at both interfaces due to lattice mismatch.

For a rhombic supercell $(m_1 \times m_1)\mathrm{G}/(m_2 \times m_2)\mathrm{SiC}$ without intercalated Gd, the corresponding ZLG-SiC lattice mismatch can be quantified by a lateral strain

$$\varepsilon_{\mathrm{G}} = \frac{m_2\sqrt{3}a_{\mathrm{SiC}} - m_1 a_{\mathrm{G}}}{m_1 a_{\mathrm{G}}} \times 100\%, \tag{3}$$

where a_{G} is the equilibrium lattice constant of freestanding graphene. A positive strain ($\varepsilon_{\mathrm{G}} > 0$) indicates that ZLG is under tensile strain, meaning it is stretched relative to a freestanding graphene sheet, while a negative strain ($\varepsilon_{\mathrm{G}} < 0$) implies compression. Specifically, using our DFT-calculated values of $a_{\mathrm{SiC}} = 3.09545$ Å and $a_{\mathrm{G}} = 2.464$ Å [29,47], the corresponding ε_{G} values for the supercells $(2 \times 2)\mathrm{G}/(1 \times 1)\mathrm{SiC}$ with $m_1 = 2$ and $m_2 = 1$, $(4 \times 4)\mathrm{G}/(2 \times 2)\mathrm{SiC}$ with $m_1 = 4$ and $m_2 = 2$, and $(13 \times 13)\mathrm{G}/(6 \times 6)\mathrm{SiC}$ with $m_1 = 13$ and $m_2 = 6$ are about +8.8%, +8.8%, and +0.4%, respectively, as listed in column 2 of Table 2. Previous experimental observations have shown that one 13×13 graphene unit cell ($m_1 = 13$) matches three 6×6 SiC(0001) unit cells ($m_2 = 6$) [33]. This implies that the thermodynamically most preferred structures observed in experiments tend to adopt the lowest strain, $\varepsilon_{\mathrm{G}} \approx +0.4\%$.

As described in Section 3.2, we construct the initial intercalated Gd configuration using a uniformly arranged $n_1 \times n_2$ Gd planar array. If $n_1 = n_2 = l$, the resulting $l \times l$ Gd array corresponds to a strained hcp Gd(0001) slab with a lateral lattice constant of $a_0^* = m_2\sqrt{3}a_{\mathrm{SiC}}/l$ and a thickness L, in a general supercell of $(m_1 \times m_1)\mathrm{G}/(m_2 \times m_2)\mathrm{SiC}$. For such an intercalated $l \times l$ Gd(0001) slab, the Gd-substrate lattice mismatch can be expressed by the lateral strain

$$\varepsilon_{\mathrm{Gd}} = \frac{m_2\sqrt{3}a_{\mathrm{SiC}} - l a_0}{l a_0} \times 100\%, \tag{4}$$

where a_0 is the equilibrium lateral lattice constant of the unstrained freestanding Gd(0001) slab. A positive strain ($\varepsilon_{\mathrm{Gd}} > 0$) implies that the Gd is under tensile strain, meaning it is stretched relative to its unstrained state, while a negative strain ($\varepsilon_{\mathrm{Gd}} < 0$) indicates compression. Using our DFT-calculated values of $a_0 = 3.384$ Å for a Gd(0001) monolayer ($L = 1$ slab) and $a_0 = 3.595$ Å for a bulk Gd(0001) slab ($L = \infty$), the corresponding $\varepsilon_{\mathrm{Gd}}$ values for the specified $l \times l$ configurations are listed in columns 5 and 6 of Table 2 for the three supercells: (2×2)G/(1×1)SiC, (4×4)G/(2×2)SiC, and (13×13)G/(6×6)SiC.

Table 2. Strain ε_{G} in graphene and $\varepsilon_{\mathrm{Gd}}$ in $l \times l$ Gd(0001) slab relative to SiC(0001) along the $\sqrt{3}a_{\mathrm{SiC}} \times \sqrt{3}a_{\mathrm{SiC}}$ unit cell for three types of supercells, calculated from Eqs. 3 and 4, with the lattice constants: $a_{\mathrm{SiC}} = 3.09545$ Å for SiC(0001) substrate [29], $a_{\mathrm{G}} = 2.464$ Å for freestanding graphene [47], $a_0 = 3.384$ Å for a Gd(0001) monolayer, and $a_0 = 3.595$ Å for a bulk Gd(0001) slab (from Appendix A). The strained lateral lattice constant of the Gd(0001) slab is calculated as $a_0^* = m_2\sqrt{3}a_{\mathrm{SiC}}/l$.

Supercell $(m_1 \times m_1)$G/$(m_2 \times m_2)$SiC	Graphene ε_{G}	Gd array $l \times l$	a_0^* (Å)	Gd(0001) monolayer $\varepsilon_{\mathrm{Gd}}$	Gd(0001) bulk slab $\varepsilon_{\mathrm{Gd}}$
(2×2)G/(1×1)SiC	+8.8%	1×1	5.361	+58.4%	+49.1%
		2×2	2.681	-20.8%	-25.4%
(4×4)G/(2×2)SiC	+8.8%	1×1	10.723	+216.9%	+198.3%
		2×2	5.361	+58.4%	+49.1%
		3×3	3.574	+5.6%	-0.6%
		4×4	2.681	-20.8%	-25.4%
(13×13)G/(6×6)SiC	+0.4%	1×1	32.169	+850.6%	+794.8%
		2×2	16.084	+375.3%	+347.4%
		3×3	10.723	+216.9%	+198.3%
		4×4	8.042	+137.7%	+123.7%
		5×5	6.434	+90.1%	+79.0%
		6×6	5.361	+58.4%	+49.1%
		7×7	4.596	+35.8%	+27.8%
		8×8	4.021	+18.8%	+11.9%
		9×9	3.574	+5.6%	-0.6%
		10×10	3.217	-4.9%	-10.5%
		11×11	2.924	-13.6%	-18.7%
		12×12	2.681	-20.8%	-25.4%

Appendix C: DFT data of 201 configurations

DFT data for Gd intercalation (175 configurations) under and adsorption (26 configurations) on top of ZLG on SiC(0001) are listed in Table 3 and Table 4, respectively. It is instructive to consider the scenario of structures with comparable chemical potentials. For example, in Table 3, examine the three structures listed for $\theta = 0.3889$. The corresponding chemical potentials, which are lower than those for other θ values, differ by approximately 0.02 eV. This difference is only slightly higher than the thermal energy $k_{\mathrm{B}}T \approx 0.007$ eV at liquid nitrogen temperatures of about 80 K. Therefore, the equilibrium layer structure is expected to consist of a mixture of these slightly different (but similarly disordered and amorphous-like) structures at liquid nitrogen temperatures.

Table 3. DFT data of 175 configurations for intercalated Gd fully relaxed by using the $(13 \times 13)\mathrm{G}/(6 \times 6)\mathrm{SiC}$ supercell (see Fig. 1) with 108 Si atoms in STL per supercell. N_{Gd} is the number of Gd atoms in intercalated Gd structure under ZLG per supercell. The coverage of Gd is defined as $\theta = N_{\mathrm{Gd}}/108$. M is the magnetic moment in unit of Bohr magneton μ_{B} per supercell. The chemical potentials μ and μ^* (in eV per Gd atom) are calculated from Eqs. 1 and 2, respectively. $n_1 \times n_2$ denotes the size of a Gd monolayer per supercell for initial configuration, where the Gd monolayer is uniformly arranged as a Gd array along $\boldsymbol{a_1}$ and $\boldsymbol{a_2}$ directions (see Fig. 1), i.e., a 2D Bravais lattice with a $6\sqrt{3}a_{\mathrm{SiC}}/n_1 \times 6\sqrt{3}a_{\mathrm{SiC}}/n_2$ rhombic primitive cell containing n_{p} Gd atoms. L is the thickness of intercalated Gd slab, in units of Gd monolayers, i.e., the intercalated Gd slab in an initial configuration consists of stacked $n_1 \times n_2$ Gd monolayers. The final column briefly lists the most basic feature of each fully relaxed configuration.

						Initial configuration			Final configuration
N_{Gd}	θ	Label	M	μ	μ^*	$n_1 \times n_2$	n_{p}	L	
1	0.0093	001-01	105.00	11.430	15.794	1×1	1	1	A single Gd atom at a fcc site per supercell
		001-02	102.99	10.983	15.347	1×1	1	1	A single Gd atom at a hcp site per supercell
		001-03	99.00	11.067	15.430	1×1	1	1	A single Gd atom at a hcp site per supercell
		001-04	105.00	10.939	15.303	1×1	1	1	A single Gd atom at a hcp site per supercell
		001-05	105.00	11.425	15.789	1×1	1	1	A single Gd atom at a fcc site per supercell
		001-06	105.00	11.412	15.776	1×1	1	1	A single Gd atom at a fcc site per supercell
		001-07	105.00	10.941	15.305	1×1	1	1	A single Gd atom at a hcp site per supercell
		001-08	105.00	11.427	15.790	1×1	1	1	A single Gd atom at a fcc site per supercell
		001-09	105.00	10.950	15.313	1×1	1	1	A single Gd atom at a hcp site per supercell
		001-10	105.00	10.948	15.312	1×1	1	1	A single Gd atom at a hcp site per supercell
		001-11	105.00	10.947	15.311	1×1	1	1	A single Gd atom at a hcp site per supercell
		001-12	105.00	11.428	15.792	1×1	1	1	A single Gd atom at a fcc site per supercell
		001-13	105.00	11.424	15.788	1×1	1	1	A single Gd atom at a fcc site per supercell
		001-14	105.00	10.953	15.316	1×1	1	1	A single Gd atom at a hcp site per supercell
		001-15	105.00	10.949	15.313	1×1	1	1	A single Gd atom at a hcp site per supercell
		001-16	105.00	10.952	15.316	1×1	1	1	A single Gd atom at a hcp site per supercell
		001-17	105.00	10.942	15.306	1×1	1	1	A single Gd atom at a hcp site per supercell
		001-18	105.00	10.936	15.300	1×1	1	1	A single Gd atom at a hcp site per supercell (Fig. 1c)
		001-19	105.00	11.428	15.792	1×1	1	1	A single Gd atom at a fcc site per supercell
		001-20	105.00	11.425	15.789	1×1	1	1	A single Gd atom at a fcc site per supercell
		001-21	105.00	10.950	15.314	1×1	1	1	A single Gd atom at a hcp site per supercell
		001-22	105.00	11.414	15.778	1×1	1	1	A single Gd atom at a fcc site per supercell
		001-23	103.00	10.981	15.345	1×1	1	1	A single Gd atom at a hcp site per supercell
		001-24	105.00	10.937	15.300	1×1	1	1	A single Gd atom at a hcp site per supercell
		001-25	105.00	10.945	15.309	1×1	1	1	A single Gd atom at a hcp site per supercell
4	0.0370	004-01	96.00	-1.488	2.876	2×2	1	1	A nearly perfect 2×2 array monolayer per supercell

		004-02	96.00	-1.943	2.420	2×2	1	1	A nearly perfect 2×2 array monolayer per supercell (Fig. 2a)
		004-03	96.00	-1.842	2.522	2×2	1	1	A nearly perfect 2×2 array monolayer per supercell
9	0.0833	009-01	81.00	-3.908	0.455	3×3	1	1	A nearly perfect 3×3 array monolayer per supercell
		009-02	81.00	-4.372	-0.008	3×3	1	1	A nearly perfect 3×3 array monolayer per supercell (Fig. 2b)
		009-03	76.78	-4.180	0.184	3×3	1	1	A nearly perfect 3×3 array monolayer per supercell
12	0.1111	012-01	65.89	-4.712	-0.348	3×4	1	1	A distorted 3×4 array monolayer per supercell
		012-02	64.14	-4.716	-0.352	3×4	1	1	A distorted 3×4 array monolayer per supercell
		012-03	66.15	-4.808	-0.444	3×4	1	1	A distorted 3×4 array monolayer per supercell (Fig. 2c)
15	0.1389	015-01	54.94	-5.138	-0.774	3×5	1	1	A distorted 3×5 array monolayer per supercell
		015-02	54.87	-5.151	-0.788	3×5	1	1	A distorted 3×5 array monolayer per supercell (Fig. 2d)
		015-03	53.10	-5.107	-0.743	3×5	1	1	A distorted 3×5 array monolayer per supercell
16	0.1481	016-01	50.01	-5.302	-0.938	4×4	1	1	A distorted 4×4 array monolayer per supercell
		016-02	48.14	-5.077	-0.713	4×4	1	1	A distorted 4×4 array monolayer per supercell
		016-03	47.97	-5.411	-1.047	4×4	1	1	A distorted 4×4 array monolayer per supercell (Fig. 2e)
18	0.1667	018-01	42.05	-5.516	-1.152	3×6	1	1	A distorted 3×6 array monolayer per supercell
		018-02	44.15	-5.604	-1.240	3×6	1	1	A nearly perfect 3×6 array monolayer per supercell (Fig. 2f)
		018-03	48.00	-5.427	-1.063	3×6	1	1	A distorted 3×6 array monolayer per supercell
20	0.1852	020-01	34.00	-5.630	-1.266	4×5	1	1	An amorphous-like monolayer (Fig. 2g)
		020-02	36.00	-5.601	-1.237	4×5	1	1	An amorphous-like monolayer
		020-03	36.00	-5.605	-1.241	4×5	1	1	An amorphous-like monolayer
21	0.1944	021-01	41.00	-5.703	-1.339	3×7	1	1	A chain-array-like monolayer (Fig. 2h)
		021-02	45.00	-5.673	-1.309	3×7	1	1	A chain-array-like monolayer
		021-03	43.00	-5.685	-1.321	3×7	1	1	A chain-array-like monolayer
24	0.2222	024-01	48.00	-5.697	-1.333	3×8	1	1	A chain-array-like monolayer
		024-02	42.01	-5.732	-1.368	3×8	1	1	A chain-array-like monolayer
		024-03	46.00	-5.708	-1.344	3×8	1	1	A chain-array-like monolayer
		024-04	22.00	-5.724	-1.360	4×6	1	1	A chain-array-like monolayer
		024-05	24.01	-5.878	-1.514	4×6	1	1	A chain-array-like monolayer (Fig. 2i)
		024-06	26.00	-5.872	-1.508	4×6	1	1	A chain-array-like monolayer
25	0.2315	025-01	16.96	-5.932	-1.568	5×5	1	1	A mottled-like monolayer
		025-02	21.00	-5.910	-1.546	5×5	1	1	A mottled-like monolayer
		025-03	19.07	-5.935	-1.571	5×5	1	1	A mottled-like monolayer (Fig. 2j)
27	0.2500	027-01	40.83	-5.808	-1.445	3×9	1	1	A locally chain- or amorphous-like monolayer (Fig. 2k)
		027-02	38.96	-5.783	-1.419	3×9	1	1	A locally chain- or amorphous-like monolayer
		027-03	39.00	-5.789	-1.425	3×9	1	1	A locally chain- or amorphous-like monolayer
28	0.2593	028-01	23.86	-5.963	-1.600	4×7	1	1	A locally chain- or amorphous-like monolayer (Fig. 2l)
		028-02	20.10	-5.918	-1.554	4×7	1	1	A locally chain- or amorphous-like monolayer
		028-03	18.09	-5.919	-1.555	4×7	1	1	A locally chain- or amorphous-like monolayer
30	0.2778	030-01	32.03	-5.856	-1.493	3×10	1	1	A locally stripe- or chain-like monolayer
		030-02	33.88	-5.869	-1.505	3×10	1	1	A locally stripe- or chain-like monolayer
		030-03	37.67	-5.858	-1.494	3×10	1	1	A locally stripe- or chain-like monolayer
		030-04	8.28	-6.003	-1.639	5×6	1	1	A locally stripe- or chain-like monolayer
		030-05	6.02	-6.003	-1.639	5×6	1	1	A locally stripe- or chain-like monolayer
		030-06	6.83	-6.017	-1.654	5×6	1	1	A locally stripe- or chain-like monolayer (Fig. 2m)
32	0.2963	032-01	22.03	-5.996	-1.632	4×8	1	1	A locally stripe- or chain-like monolayer
		032-02	24.01	-5.964	-1.600	4×8	1	1	A locally stripe- or chain-like monolayer
		032-03	23.63	-5.996	-1.632	4×8	1	1	A locally stripe- or chain-like monolayer (Fig. 2n)
33	0.3056	033-01	26.99	-5.944	-1.580	3×11	1	1	A locally stripe- or amorphous-like monolayer
		033-02	25.00	-5.945	-1.581	3×11	1	1	A locally stripe- or amorphous-like monolayer
		033-03	27.00	-5.988	-1.624	3×11	1	1	A locally stripe- or amorphous-like monolayer (Fig. 2o)
35	0.3241	035-01	1.05	-6.160	-1.797	5×7	1	1	An amorphous-like monolayer
		035-02	1.19	-6.171	-1.807	5×7	1	1	An amorphous-like monolayer (Fig. 2p)
		035-03	1.14	-6.169	-1.805	5×7	1	1	An amorphous-like monolayer
36	0.3333	036-01	12.14	-5.695	-1.331	6×6	1	1	A nearly perfect Gd(0001) monolayer
		036-02	4.00	-6.078	-1.714	6×6	1	1	A nearly perfect Gd(0001) monolayer (Fig. 5a)
		036-03	12.00	-6.066	-1.702	6×6	1	1	An amorphous-like monolayer
		036-04	16.00	-6.032	-1.668	4×9	1	1	An amorphous-like monolayer
		036-05	18.00	-6.014	-1.650	4×9	1	1	An amorphous-like monolayer
		036-06	20.00	-6.033	-1.669	4×9	1	1	An amorphous-like monolayer
40	0.3704	040-01	14.00	-6.048	-1.684	4×10	1	1	An amorphous-like monolayer
		040-02	14.00	-6.064	-1.701	4×10	1	1	An amorphous-like monolayer

		040-03	14.00	-6.071	-1.707	4×10	1	1	An amorphous-like monolayer
		040-04	6.00	-6.150	-1.787	5×8	1	1	An amorphous-like monolayer
		040-05	11.98	-6.108	-1.744	5×8	1	1	An amorphous-like monolayer
		040-06	6.00	-6.177	-1.813	5×8	1	1	An amorphous-like monolayer (Fig. 5b)
42	0.3889	042-01	0.32	-6.219	-1.855	6×7	1	1	An amorphous-like monolayer
		042-02	1.98	-6.238	-1.874	6×7	1	1	An amorphous-like monolayer (Fig. 6a)
		042-03	0.09	-6.212	-1.848	6×7	1	1	An amorphous-like monolayer
44	0.4074	044-01	10.01	-6.068	-1.704	4×11	1	1	An amorphous-like monolayer
		044-02	9.99	-6.071	-1.707	4×11	1	1	An amorphous-like monolayer
		044-03	10.00	-6.111	-1.747	4×11	1	1	An amorphous-like monolayer (Fig. 5c)
45	0.4167	045-01	3.05	-6.185	-1.822	5×9	1	1	An amorphous-like monolayer (Fig. 5d)
		045-02	3.04	-6.148	-1.784	5×9	1	1	An amorphous-like monolayer
		045-03	3.00	-6.185	-1.821	5×9	1	1	An amorphous-like monolayer
48	0.4444	048-01	0.00	-6.150	-1.786	6×8	1	1	An amorphous-like monolayer
		048-02	0.00	-6.195	-1.831	6×8	1	1	An amorphous-like monolayer (Fig. 5e)
		048-03	0.00	-6.190	-1.826	6×8	1	1	An amorphous-like monolayer
49	0.4537	049-01	0.78	-6.186	-1.822	7×7	1	1	An amorphous-like monolayer (Fig. 5f)
		049-02	0.84	-6.164	-1.800	7×7	1	1	An amorphous-like monolayer
		049-03	0.82	-6.176	-1.812	7×7	1	1	An amorphous-like monolayer
50	0.4630	050-01	0.00	-6.202	-1.839	5×10	1	1	An amorphous-like monolayer (Fig. 5g)
		050-02	2.34	-6.192	-1.828	5×10	1	1	An amorphous-like monolayer
		050-03	2.00	-6.169	-1.806	5×10	1	1	An amorphous-like monolayer
54	0.5000	054-01	0.00	-6.185	-1.821	6×9	1	1	An amorphous-like monolayer
		054-02	0.00	-6.197	-1.834	6×9	1	1	An amorphous-like monolayer (Fig. 5h)
		054-03	0.00	-6.172	-1.808	6×9	1	1	An amorphous-like monolayer
55	0.5093	055-01	0.99	-6.133	-1.769	5×11	1	1	An amorphous-like monolayer
		055-02	1.00	-6.132	-1.768	5×11	1	1	An amorphous-like monolayer
		055-03	0.48	-6.141	-1.777	5×11	1	1	An amorphous-like monolayer (Fig. 5i)
56	0.5185	056-01	0.00	-6.127	-1.764	7×8	1	1	An amorphous-like monolayer
		056-02	0.00	-6.156	-1.792	7×8	1	1	An amorphous-like monolayer (Fig. 5j)
		056-03	0.00	-6.145	-1.782	7×8	1	1	An amorphous-like monolayer
60	0.5556	060-01	0.00	-6.104	-1.740	6×10	1	1	An amorphous-like monolayer
		060-02	0.00	-6.127	-1.763	6×10	1	1	An amorphous-like monolayer (Fig. 5k)
		060-03	0.00	-6.096	-1.733	6×10	1	1	An amorphous-like monolayer
63	0.5833	063-01	0.05	-6.119	-1.755	7×9	1	1	An amorphous-like monolayer
		063-02	0.08	-6.127	-1.763	7×9	1	1	An amorphous-like monolayer
		063-03	0.66	-6.139	-1.775	7×9	1	1	An amorphous-like monolayer (Fig. 5l)
64	0.5926	064-01	0.00	-6.052	-1.689	8×8	1	1	An amorphous-like monolayer
		064-02	0.00	-6.087	-1.723	8×8	1	1	An amorphous-like monolayer
		064-03	0.00	-6.092	-1.728	8×8	1	1	An amorphous-like monolayer (Fig. 5m)
66	0.6111	066-01	0.00	-6.074	-1.711	6×11	1	1	An amorphous-like monolayer (Fig. 5n)
		066-02	0.00	-6.066	-1.702	6×11	1	1	An amorphous-like monolayer
		066-03	0.00	-6.043	-1.679	6×11	1	1	An amorphous-like monolayer
70	0.6481	070-01	0.00	-6.038	-1.674	7×10	1	1	An amorphous-like monolayer
		070-02	0.00	-6.062	-1.698	7×10	1	1	An amorphous-like monolayer (Fig. 5o)
		070-03	0.00	-6.032	-1.668	7×10	1	1	An amorphous-like monolayer
72	0.6667	072-01	0.00	-6.014	-1.650	6×6[a]	2	1	An amorphous-like monolayer
		072-02	0.00	-5.534	-1.170	6×6[a]	2	1	A gadolinene-like monolayer
		072-03	0.00	-6.027	-1.663	6×6[a]	2	1	An amorphous-like monolayer
		072-04	0.00	-6.054	-1.690	8×9	1	1	An amorphous-like monolayer (Fig. 5p)
		072-05	0.00	-5.968	-1.604	8×9	1	1	An amorphous-like monolayer with bumps
		072-06	0.00	-5.986	-1.622	8×9	1	1	An amorphous-like monolayer
77	0.7130	077-01	0.47	-5.929	-1.565	7×11	1	1	An amorphous-like monolayer
		077-02	0.39	-5.982	-1.619	7×11	1	1	An amorphous-like monolayer (Fig. 7a)
		077-03	0.78	-5.937	-1.573	7×11	1	1	An amorphous-like monolayer
80	0.7407	080-01	0.00	-5.901	-1.537	8×10	1	1	An amorphous-like monolayer
		080-02	0.00	-5.941	-1.577	8×10	1	1	An amorphous-like monolayer (Fig. 7b)
		080-03	0.00	-5.885	-1.521	8×10	1	1	An amorphous-like monolayer
81	0.7500	081-01	0.56	-5.889	-1.525	9×9	1	1	An amorphous-like monolayer (Fig. 7c)
		081-02	0.43	-5.874	-1.510	9×9	1	1	An amorphous-like monolayer
		081-03	0.62	-5.846	-1.482	9×9	1	1	An amorphous-like monolayer
84	0.7778	084-01	0.00	-5.855	-1.491	6×7[b]	1	2	A locally Gd(0001)- or amorphous-like monolayer (Fig. 7d)
		084-02	0.00	-5.825	-1.461	6×7[b]	1	2	A locally Gd(0001)- or amorphous-like monolayer
		084-03	0.00	-5.688	-1.324	6×7[b]	1	2	An amorphous-like monolayer with bumps
88	0.8148	088-01	0.00	-5.742	-1.378	8×11	1	1	An amorphous-like monolayer (Fig. 7e)
		088-02	0.00	-5.686	-1.322	8×11	1	1	An amorphous-like monolayer
		088-03	0.00	-5.709	-1.346	8×11	1	1	An amorphous-like monolayer

90	0.8333	090-01	0.00	-5.724	-1.360	9×10	1	1	A locally Gd(0001)- or amorphous-like monolayer (Fig. 7f)
		090-02	0.00	-5.692	-1.329	9×10	1	1	A locally Gd(0001)- or amorphous-like monolayer
		090-03	0.00	-5.696	-1.332	9×10	1	1	A Gd(0001)-like monolayer with vacancies
98	0.9074	098-01	0.00	-5.299	-0.935	7×7[c]	1	2	A Gd(0001)-like monolayer with bumps
		098-02	1.85	-5.404	-1.040	7×7[c]	1	2	A locally Gd(0001)- or amorphous-like monolayer with bumps
		098-03	0.00	-5.412	-1.048	7×7[c]	1	2	A locally Gd(0001)- or amorphous-like monolayer with bumps (Fig. 7g)
99	0.9167	099-01	0.87	-5.505	-1.141	9×11	1	1	A Gd(0001)-like monolayer with vacancies
		099-02	0.44	-5.534	-1.171	9×11	1	1	A Gd(0001)-like monolayer with vacancies (Fig. 7h)
		099-03	0.49	-5.469	-1.105	9×11	1	1	A Gd(0001)-like monolayer with vacancies and bumps
100	0.9259	100-01	0.00	-5.518	-1.154	10×10	1	1	A Gd(0001)-like monolayer with vacancies
		100-02	0.00	-5.514	-1.150	10×10	1	1	A Gd(0001)-like monolayer with vacancies
		100-03	0.00	-5.558	-1.195	10×10	1	1	A Gd(0001)-like monolayer with vacancies (Fig. 7i)
108	1.0000	108-01	0.00	-5.026	-0.662	6×6[d]	3	1	A nearly perfect Gd(0001) monolayer
		108-02	0.00	-5.415	-1.051	6×6[d]	3	1	A nearly perfect Gd(0001) monolayer (Fig. 7j)
		108-03	0.00	-5.314	-0.950	6×6[d]	3	1	An Gd(0001)-like monolayer with bumps
110	1.0185	110-01	0.00	-5.299	-0.935	10×11	1	1	A Gd(0001)-like monolayer with bumps (Fig. 7k)
		110-02	0.00	-5.298	-0.934	10×11	1	1	A Gd(0001)-like monolayer with bumps
		110-03	0.00	-5.292	-0.928	10×11	1	1	A Gd(0001)-like monolayer with bumps
121	1.1204	121-01	2.84	-5.099	-0.736	11×11	1	1	An amorphous-like multilayer (Fig. 7l)
		121-02	0.97	-5.078	-0.714	11×11	1	1	An amorphous-like multilayer
		121-03	1.01	-5.083	-0.719	11×11	1	1	An amorphous-like multilayer

[a]A 6 × 6 gadolinene (honeycomb) layer.
[b]An AB stacked 6 × 7 Gd array bilayer.
[c]An AB stacked 7 × 7 Gd array bilayer.
[d]A $6\sqrt{3}a^*_{\mathrm{Gd}} \times 6\sqrt{3}a^*_{\mathrm{Gd}}$ Gd(0001) monolayer with the lattice constant $a^*_{\mathrm{Gd}} = a_{\mathrm{SiC}}$.

Table 4. DFT data of 26 configurations for supported Gd fully relaxed by using the $(13 \times 13)\mathrm{G}/(6 \times 6)\mathrm{SiC}$ supercell (see Fig. 1) with 108 Si atoms in STL per supercell. N_{Gd} is the number of Gd atoms in Gd structure adsorbed on top of ZLG per supercell. See the caption of Table 3 for definitions of other quantities.

N_{Gd}	θ	Label	M	μ	μ^*	Final configuration
1	0.0093	001-01	1.00	-3.681	0.683	A single Gd atom at a site nearby a C ring center
		001-02	0.78	-3.501	0.863	A single Gd atom at a site nearby a C ring center
		001-03	13.01	-3.372	0.992	A single Gd atom at a site nearby a C-C bridge site
		001-04	0.91	-2.681	1.682	A single Gd atom at a locally low C top site
		001-05	5.00	-3.442	0.921	A single Gd atom at a site in the middle from a C to its ring center
		001-06	3.01	-2.970	1.394	A single Gd atom at a locally low C top site
		001-07	13.00	-3.953	0.411	A single Gd atom at a site nearby a C-C bridge site
		001-08	3.03	-2.712	1.652	A single Gd atom at a C top site
		001-09	5.00	-3.417	0.946	A single Gd atom at a C ring center
		001-10	3.07	-3.865	0.499	A single Gd atom at a locally low C-C bridge site
		001-11	0.66	-3.512	0.852	A single Gd atom at a locally low C top site
		001-12	0.41	-3.087	1.277	A single Gd atom at a site nearby a C ring center
		001-13	7.00	-3.284	1.079	A single Gd atom at a site nearby a C ring center
		001-14	0.70	-3.608	0.755	A single Gd atom at a site nearby a C ring center
		001-15	5.00	-3.162	1.201	A single Gd atom at a locally low C-C bridge site
		001-16	0.08	-4.186	0.177	A single Gd atom at a locally low C-C bridge site
		001-17	13.18	-4.230	0.133	A single Gd atom at a locally low C-C bridge site
		001-18	0.99	-2.951	1.413	A single Gd atom at a locally low C-C bridge site
		001-19	3.29	-3.897	0.467	A single Gd atom at a locally low C-C bridge site
		001-20	3.53	-3.634	0.730	A single Gd atom at a site nearby a C ring center
		001-21	5.00	-3.982	0.382	A single Gd atom at a site nearby a C ring center
		001-22	1.00	-3.176	1.188	A single Gd atom at a site nearby a C ring center
		001-23	4.22	-4.283	0.081	A single Gd atom at a locally low C-C bridge site (Fig. 1d)
		001-24	2.63	-3.495	0.869	A single Gd atom at a site in the middle from a C to its ring center
		001-25	3.09	-3.503	0.861	A single Gd atom at a locally low C-C bridge site
42	0.3889	042-02	0.00	-3.964	0.400	An amorphous-like monolayer (Fig. 6b)

References

[1] X. Zhao, P. Song, C. Wang, A.C. Riis-Jensen, W. Fu, Y. Deng, D. Wan, L. Kang, S. Ning, J. Dan, T. Venkatesan, Z. Liu, W. Zhou, K.S. Thygesen, X. Luo, S.J. Pennycook, K.P. Loh, Engineering covalently bonded 2D layered materials by self-intercalation, Nature 581, (2020) 171–177.

[2] J. Wan, S.D. Lacey, J. Dai, W. Bao, M.S. Fuhrer, L. Hu, Tuning two-dimensional nanomaterials by intercalation: materials, properties and applications, Chem. Soc. Rev. 45 (2016) 6742–6765.

[3] L. Daukiya, M.N. Nair, M. Cranney, F. Vonau, S. Hajjar-Garreau, D. Aubel, L. Simon, Functionalization of 2D materials by intercalation, Prog. Surf. Sci. 94 (2019) 1–20.

[4] M.S. Stark, K.L. Kuntz, S.J. Martens, S.C. Warren, Intercalation of layered materials from bulk to 2D, Adv. Mater. 31 (2019) 1808213.

[5] N. Briggs, Z.M. Gebeyehu, A. Vera, T. Zhao, K. Wang, A.D.L.F. Duran, B. Bersch, T. Bowen, K.L. Knappenberger, J.A. Robinson, Epitaxial graphene/silicon carbide intercalation: a minireview on graphene modulation and unique 2D materials, Nanoscale 11, (2019) 15440–15447.

[6] E. Mazaleyrat, S. Vlaic, A. Artaud, L. Magaud, T. Vincent, A.C. Gómez-Herrero, S. Lisi, P. Singh, N. Bendiab, V. Guisset, P. David, S. Pons, D. Roditchev, C. Chapelier, J. Coraux, How to induce superconductivity in epitaxial graphene via remote proximity effect through an intercalated gold layer, 2D Mater. 8 (2020) 015002.

[7] Nathaniel A. Anderson, M. Hupalo, D. Keavney, M. Tringides, D. Vaknin, Intercalated rare-earth metals under graphene on SiC, J. Mag. Mag. Mater. 474 (2019) 666–670.

[8] S. Link, S. Forti, A. Stöhr, K. Küster, M. Rösner, D. Hirschmeier, C. Chen, J. Avila, M.C. Asensio, A.A. Zakharov, T.O. Wehling, A.I. Lichtenstein, M.I. Katsnelson, U. Starke, Introducing strong correlation effects into graphene by gadolinium intercalation, Phys. Rev. B 100 (2019) 121407.

[9] M. Kolmer, B. Schrunk, M. Hupalo, J. Hall, S. Chen, J. Zhang, C.-Z. Wang, A. Kaminski, M. C. Tringides, Highly asymmetric graphene layer doping and band structure manipulation in rare earth–graphene heterostructure by targeted bonding of the intercalated gadolinium, J. Phys. Chem. C 126 (2022) 6863–6873.

[10] M. Kolmer, W. Ko, J. Hall, S. Chen, J. Zhang, H. Zhao, L. Ke, C.-Z Wang, A.-P. Li, M.C. Tringides, Breaking of inversion symmetry and interlayer electronic coupling in bilayer graphene heterostructure by structural implementation of high electric displacement fields, J. Phys. Chem. Lett. 13 (2022), 11571–11580.

[11] A.C. Qu, P. Nigge, S. Link, G. Levy, M. Michiardi, P.L. Spandar, T. Matthé, M. Schneider, S. Zhdanovich, U. Starke, C. Gutiérrez, A. Damascelli, Ubiquitous defect-induced density wave instability in monolayer graphene, Sci. Adv. 8 (2022) eabm5180.

[12] K. Idczak, E. Wachowicz, Influence of intercalated Gd atoms on graphene-4H-SiC(0001) properties, Appl. Surf. Sci. 609 (2023) 155365.

[13] C. Wang, K. Wang, H. Wang, Q. Tian, J. Zong, X. Qiu, W. Ren, L. Wang, F.-S. Li, W.-B. Zhang, H. Zhang, Y. Zhang, Observation of a folded Dirac cone in heavily doped graphene, J. Phys. Chem. Lett. 14 (2023) 7149–7156.

[14] M. Kim, M. Hupalo, M. C. Tringides, B. Schrunk, A. Kaminski, K.-M. Ho, C.-Z. Wang, Electronic structure of double-layer epitaxial graphene on SiC(0001) modified by Gd intercalation, J. Phys. Chem. C 124 (2020) 28132–28138.

[15] J.G. Checkelsky, B.A. Bernevig, P. Coleman, Q. Si, S. Paschen, Flat bands, strange metals and the Kondo effect, Nat. Rev. Mater. 9 (2024) 509–526.

[16] Y. Han, S. Chen, J. Hall, S. Roberts, M. Kolmer, J.W. Evans, M.C. Tringides, Degeneracy in intercalated Pb phases under buffer-layer graphene on SiC(0001) and diffuse moiré spots in surface diffraction, J. Phys. Chem. Lett. 14 (2023) 7053–7058.

[17] Y. Han, M. Kolmer, J.W. Evans, M.C. Tringides, First-principles analysis of intercalated Pb structures under buffer-layer graphene on SiC(0001): Pb(111)-, plumbene-, and amorphous-like Pb layers, Phys. Rev. Mater. 8 (2024) 044002.

[18] C. Wang, T. Cheng, Z. Liu, F. Liu, H. Huang, Structural amorphization-induced topological order, Phys. Rev. Lett. 128 (2022) 056401.

[19] Y. Han, A. Lii-Rosales, Y. Zhou, C.-J. Wang, M. Kim, M.C. Tringides, C.-Z. Wang, P.A. Thiel, J.W. Evans, Nucleation and growth kinetics for intercalated islands during deposition on layered materials with isolated pointlike surface defects, Phys. Rev. Mater. 1 (2017) 053403.

[20] Y. Han, A. Lii-Rosales, M.C. Tringides, J.W. Evans, Competitive formation of intercalated versus supported metal nanoclusters during deposition on layered materials with surface point defects, J. Chem. Phys. 154 (2021) 024703.

[21] Y. Han, M. Kolmer, M.C. Tringides, J.W. Evans, Thermodynamics and kinetics of Pb intercalation under graphene on SiC(0001), Carbon 205 (2023) 336–344.

[22] L.-L. Wang, S. Chen, M. Kolmer, Y. Han, M.C. Tringides, Strain-modulated intercalated phases of Pb monolayer with dual periodicity in SiC(0001)-graphene interface, Appl. Surf. Sci. 681 (2025) 161572.

[23] S. Chen, Y. Han, M. Kolmer, J. Hall, M. Hupalo, J.W. Evans, M. C. Tringides, Targeted Dy intercalation under graphene/SiC for tuning its electronic band structure, Phys. Rev. B 107 (2023) 045408.

[24] D. McDougall, H. Hattab, M.T. Hershberger, M. Hupalo, M.H. von Hoegen, P.A. Thiel, M.C. Tringides, Dy uniform film morphologies on graphene studied with SPA-LEED and STM, Carbon 108 (2016) 283–290.

[25] X. Liu, C.-Z. Wang, M. Hupalo, H.-Q. Lin, K.-M. Ho, M. C. Tringides, Metals on graphene: interactions, growth morphology, and thermal stability, Crystals 3 (2013) 79–111.

[26] G. Kresse, J. Furthmüller, Efficient iterative schemes for ab initio total-energy calculations using a plane-wave basis set, Phys. Rev. B 54 (1996) 11169–11186.

[27] G. Kresse, D. Joubert, From ultrasoft pseudopotentials to the projector augmented-wave method, Phys. Rev. B 59 (1999) 1758–1775.

[28] J. Klimeš, D.R. Bowler, A. Michaelides, Chemical accuracy for the van der Waals density functional, J. Phys. Condens. Mat. 22 (2010) 022201.

[29] Y. Han, J.W. Evans, M.C. Tringides, Dy adsorption on and intercalation under graphene on 6*H*-SiC(0001) surface from first-principles calculations, Phys. Rev. Mater. 5 (2021) 074004.

[30] Y. Han, J.W. Evans, M.C. Tringides, Energy barriers for Dy and H penetrating graphene on 6*H*-SiC(0001) and freestanding bilayer graphene from first-principles calculations, Appl. Phys. Lett. 119 (2021) 033101.

[31] I. Forbeaux, J.-M. Themlin, and J.-M. Debever, Heteroepitaxial graphite on 6*H*-SiC(0001): Interface formation through conduction-band electronic structure, Phys. Rev. B 58 (1998) 16396–16406.

[32] T. Ohta, A. Bostwick, T. Seyller, K. Horn, E. Rotenberg, Controlling the electronic structure of bilayer graphene, Science 313 (2006) 951–954.

[33] J. Hass, W.A. de Heer, E.H. Conrad, The growth and morphology of epitaxial multilayer graphene, J. Phys. Condens. Mat. 20 (2008) 323202.

[34] W. Li, L. Huang, M.C. Tringides, J.W. Evans, Y. Han, Thermodynamic preference for atom adsorption on versus intercalation into multilayer graphene, J. Phys. Chem. Lett. 11 (2020) 9725–9730.

[35] M. Kolmer, J. Hall, S. Chen, S. Roberts, Z. Fei, Y. Han, M.C. Tringides, Atomic-scale manipulation of buried graphene–silicon carbide interface by local electric field, Commun. Phys. 7 (2024) 16.

[36] K.A. Fichthorn, M. Scheffler, Island nucleation in thin-film epitaxy: a first-principles investigation, Phys. Rev. Lett. 84 (2000) 5731–5374.

[37] W. Li, L. Huang, J. W. Evans, Y. Han, Submonolayer Ag films on Fe(100): A first-principles analysis of energetics controlling adlayer thermodynamics and kinetics, Phys. Rev. B 93 (2016) 155416.

[38] R.C. Longo, V.S. Stepanyuk, J. Kirschner, Elastic adsorbate interactions at the mesoscale, J. Phys. Condens. Matter 18 (2006) 9143–9149.

[39] W. Kappus, Y. Han, DFT-based mesoscopic interactions of N adatoms on Cu(100), Surf. Sci. 736 (2023) 122330.

[40] S. Chen, P.A. Thiel, E. Conrad, M.C. Tringides, Growth and stability of Pb intercalated phases under graphene on SiC, Phys. Rev. Mater. 4 (2020) 124005.

[41] T.A. de Jong, E.E. Krasovskii, C. Ott, R.M. Tromp, S.J. van der Molen, J. Jobst, Intrinsic stacking domains in graphene on silicon carbide: A pathway for intercalation, Phys. Rev. Mater. 2 (2018) 104005.

[42] I. Palacio, A. Celis, M.N. Nair, A. Gloter, A. Zobelli, M. Sicot, D. Malterre, M.S. Nevius, W.A. de Heer, C. Berger, E.H. Conrad, A. Taleb-Ibrahimi, A. Tejeda, Atomic structure of epitaxial graphene sidewall nanoribbons: flat graphene, miniribbons, and the confinement gap, Nano Lett. 15 (2015) 182–189.

[43] L. Ferbel, S. Veronesi, A. Rossi, S. Forti, Y. Vlamidis, C. Coletti, S. Heun, Intercalated structures formed by platinum on epitaxial graphene on SiC(0001), Carbon 234 (2025) 119989.

[44] M. Hupalo, S. Binz, M.C. Tringides, Strong metal adatom–substrate interaction of Gd and Fe with graphene, J. Phys. Condens. Matter. 23 (2011) 045005.

[45] M. Hupalo, X. Liu, C.-Z. Wang, W.-C. Lu, Y.-X. Yao, K.-M. Ho, M. C. Tringides, Metal nanostructure formation on graphene: weak versus strong bonding, Adv. Mater. 23 (2011) 2082–2087.

[46] K.T. Chan, J.B. Neaton, M.L. Cohen, First-principles study of metal adatom adsorption on graphene, Phys. Rev. B 77 (2008) 235430.

[47] Y. Han, K.C. Lai, A. Lii-Rosales, M.C. Tringides, J.W. Evans, P. A. Thiel, Surface energies, adhesion energies, and exfoliation energies relevant to copper-graphene and copper-graphite systems, Surf. Sci. 685 (2019) 48–58.

[48] X. Liu, Y. Han, J.W. Evans, A.K. Engstfeld, R.J. Behm, M.C. Tringides, M. Hupalo, H.-Q. Lin, L. Huang, K.-M. Ho, D. Appy, P. A. Thiel, C.-Z. Wang, Prog. Surf. Sci. 90 (2015) 397–443.

[49] J.R. Banister, S. Legvold, F.H. Spedding, Structure of Gd, Dy, and Er at low temperatures, Phys. Rev. 94 (1954) 1140–1142.

[50] H.E. Nigh, S. Legvold, F. H. Spedding, Magnetization and electrical resistivity of gadolinium single crystals, Phys. Rev. 132 (1963) 1092–1097.

[51] K.A. Gschneidner, Physical properties and interrelationships of metallic and semimetallic elements, Solid State Phys. 16 (1964) 275–426.

[52] O.C. Trulson, D.E. Hudson, F.H. Spedding, Cohesive energies of europium, gadolinium, holmium, and erbium, J. Chem. Phys. 35 (1961) 1018–1026.

[53] F.H. Spedding, A.H. Daane, K.W. Herrmann, The crystal structures and lattice parameters of high-purity scandium, yttrium and the rare earth metals, Acta Cryst. 9 (1956) 559–563.

[54] L. Brewer, The cohesive energies of the elements, Report No. LBL-3720 Rev. (Lawrence Berkeley National Laboratory, University of California, Berkeley, 1977), https://escholarship.org/uc/item/08p2578m.